

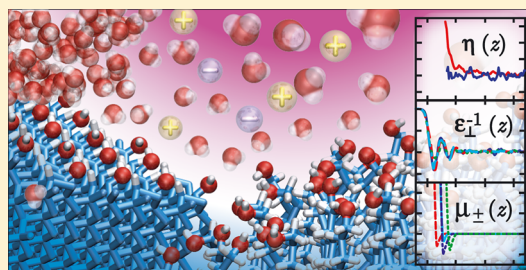
Beyond the Continuum: How Molecular Solvent Structure Affects Electrostatics and Hydrodynamics at Solid–Electrolyte Interfaces

Douwe Jan Bonthuis^{*,†} and Roland R. Netz[‡]

[†]Rudolf Peierls Centre for Theoretical Physics, University of Oxford, Oxford OX1 3NP, United Kingdom

[‡]Fachbereich Physik, Freie Universität Berlin, 14195 Berlin, Germany

ABSTRACT: Standard continuum theory fails to predict several key experimental results of electrostatic and electrokinetic measurements at aqueous electrolyte interfaces. In order to extend the continuum theory to include the effects of molecular solvent structure, we generalize the equations for electrokinetic transport to incorporate a space dependent dielectric profile, viscosity profile, and non-electrostatic interaction potential. All necessary profiles are extracted from atomistic molecular dynamics (MD) simulations. We show that the MD results for the ion-specific distribution of counterions at charged hydrophilic and hydrophobic interfaces are accurately reproduced using the dielectric profile of pure water and a non-electrostatic repulsion in an extended Poisson–Boltzmann equation. The distributions of Na^+ at both surface types and Cl^- at hydrophilic surfaces can be modeled using linear dielectric response theory, whereas for Cl^- at hydrophobic surfaces it is necessary to apply nonlinear response theory. The extended Poisson–Boltzmann equation reproduces the experimental values of the double-layer capacitance for many different carbon-based surfaces. In conjunction with a generalized hydrodynamic theory that accounts for a space dependent viscosity, the model captures the experimentally observed saturation of the electrokinetic mobility as a function of the bare surface charge density and the so-called anomalous double-layer conductivity. The two-scale approach employed here—MD simulations and continuum theory—constitutes a successful modeling scheme, providing basic insight into the molecular origins of the static and kinetic properties of charged surfaces, and allowing quantitative modeling at low computational cost.



■ INTRODUCTION

Water is the primary constituent of biological cells¹ and finds extensive use as a solvent as well as a working fluid in technological applications. In particular, the rapid advance of nanoscale fabrication techniques over the past decades has enabled the study and control of water flowing in pico- to nanoliter scale quantities, paving the way for analysis and manipulation of biological and chemical processes on a single-molecular basis.^{2–4} The small length scales that are typical of biological cells and micro- and nanofluidic devices imply that aqueous interfaces are abundant, and interactions between solutes are dominated by interfacial particularities. Despite its many anomalies, such as the pressure and temperature dependence of many of its thermodynamic properties⁵ and its wave-vector dependent dielectric oscillations,⁶ bulk water can—for most applications—be described using a spatially homogeneous static dielectric constant and viscosity. At interfaces, on the other hand, the fluid properties differ in two important aspects. First of all, interfacial water molecules exhibit a pronounced anisotropic arrangement due to their strong polarity. Vibrational spectroscopy reveals that interfacial water molecules preferentially orient with one OH bond pointing away from the liquid phase at air–water⁷ and quartz–water⁸ interfaces. This alignment effect of the aqueous boundary layer, which generally extends to about 1 nm away from the interface, gives rise to a powerful oscillatory electric

field in the interfacial region, markedly affecting the structure and dynamics of the interfacial water. Second, the water density is not homogeneous but exhibits a distinct profile instead, depending crucially on the nature of the interface. At air–water interfaces, the density increases monotonically from the air to the bulk phase. At hard solid walls, on the other hand, the density shows a high peak at the position of the first molecular layer and an oscillating profile across several subsequent layers, reaching the bulk value after about 1 nm. Similar oscillations, although less pronounced, are found at soft walls, such as lipid membranes. The two effects mentioned—orientation and spatial arrangement—primarily determine the peculiar properties of aqueous interfaces, and play an important role in the stability of colloidal suspensions,^{9,10} hydration interaction,^{11,12} protein folding and aggregation, hydrophobic interaction,¹³ and biomolecular recognition.^{14–16}

The interfacial water structure depends significantly on surface chemistry, showing particularly large qualitative differences between hydrophobic and hydrophilic surfaces. Whereas the water phase connects almost seamlessly to hydrophilic interfaces, the water density at hydrophobic interfaces shows a gap between the water and the surface.¹⁷ This difference in

Received: March 11, 2013

Revised: July 22, 2013

Published: August 8, 2013

density profiles has profound implications for the hydrodynamic properties of the interfacial layer. A second significant distinction between the two surface types concerns the affinity of different ionic species for the interface.¹⁸

Particles in aqueous solution typically carry a net surface charge density, which is compensated for by an excess of counterions in the electrolyte. In electrokinetics, this charge separation is used to drive fluid along charged surfaces by means of a tangentially applied electric field. Electrokinetic measurements provide an accurate instrument to probe the electrostatic and hydrodynamic properties of aqueous interfaces, but they require careful interpretation because of their indirect nature. The basic setup of a typical electrokinetic measurement consists of a planar interface having translational invariance in the directions parallel to the interface (x and y directions, denoted \parallel), so all quantities only depend on the direction perpendicular to the surface (z direction, denoted \perp). The force balance relates the tangential electro-osmotic velocity $u_{\parallel}(z)$ to the applied electric field E_{\parallel} and the electrostatic potential $\psi(z)$

$$\nabla\eta(z)\nabla u_{\parallel}(z) = E_{\parallel}\nabla\epsilon_0\epsilon_{\perp}(z)\nabla\psi(z) \quad (1)$$

with $\eta(z)$ being the space dependent viscosity profile, $\epsilon_{\perp}(z)$ being the perpendicular component of the relative dielectric tensor, and ϵ_0 being the vacuum permittivity. In standard continuum theory of electric double layers, the effects of water on electrostatic interactions and ion distributions are accounted for by the homogeneous dielectric function $\epsilon_{\perp}(z) = \epsilon_{\text{bulk}}$, an approximation that we refer to as the Gouy–Chapman model. Similarly, hydrodynamic friction is taken into account by means of the homogeneous viscosity $\eta(z) = \eta_{\text{bulk}}$, ignoring the interfacial water structure. A promising strategy to remedy this lack of molecular detail is to use a two-scale modeling approach: obtaining the molecular information from atomistic molecular dynamics (MD) simulations and incorporating the resulting profiles for $\eta(z)$ and $\epsilon_{\perp}(z)$ into continuum theory. This combination of atomistic simulation and continuum theory has the advantage of connecting the effects of molecular structure with the large time and length scales of continuum theory, without the expenses of separate atomistic simulations for every individual set of system parameters. In this paper, we discuss three important components of a two-scale model of an aqueous interface, highlighting multiple effects of molecular detail on the force balance in electrokinetic experiments (eq 1).

First, the dielectric tensor $\vec{\epsilon}(z)$, which expresses the response of the polar water molecules to changes in the local electric field, shows a strong spatial dependence as a result of the interfacial water structure. One of the first models that accounted for the variation of the dielectric function close to aqueous interfaces was proposed by Stern.¹⁹ On the basis of the observation that the double-layer capacitance predicted by the Gouy–Chapman theory (i.e., assuming the approximation $\epsilon_{\perp}(z) = \epsilon_{\text{bulk}}$) exceeds the experimental values by an order of magnitude, he proposed an interfacial layer of low dielectric constant. Although the Stern layer model correctly predicts electrostatic potential differences between the surface and a position far away from the interface, the dielectric profile close to the interface exhibits a more intricate pattern. In fact, the dielectric interface effect has been shown to be closely associated with the local water structure using an approximate statistical mechanical treatment.²⁰ On the linear level, electrostatic solvent effects are described in full by the nonlocal dielectric tensor.^{21,22} Recently, we have determined the local

dielectric tensor $\vec{\epsilon}(z)$ of pure water at diamond interfaces, as well as its relation to the width of the Stern layer, using MD simulations.²³ At high electric field strength (>2 V/nm), the dielectric response function becomes nonlinear,²⁴ which we show to be important for adsorption of relatively big ions at hydrophobic surfaces.

Second, the hydrodynamic boundary condition at solid–liquid interfaces depends decisively on the hydrophobicity of the surface and the associated water structure. Experiments measuring the hydrodynamic force on hydrophilic glass particles are compatible with a highly viscous interfacial water layer with a width of up to ~ 1 nm.²⁵ In agreement with these measurements, simulations show that the viscosity in the first water layers adjacent to hydrophilic surfaces exceeds the bulk viscosity.^{26,27} At hydrophobic interfaces, on the other hand, the fluid slips along the surface, which can be modeled using a finite slip length. The extent of slippage depends on the charge density²⁸ and roughness²⁷ of the solid surface, as well as pressure, impurities, and dissolved gas in the liquid phase.²⁸

Third, interactions between interfaces and ions in solution are strongly ion-specific.²⁹ Ion-specificity does not arise in the Gouy–Chapman model, because it considers point charges in a homogeneous dielectric medium. Although all contributions to the ionic free energy are essentially electrostatic in nature, they are treated on different levels in continuum macroscopic electrostatic descriptions of aqueous interfaces: the charge on the ions is used as the free charge density in the Poisson equation, the bound charge on the water molecules is included in the dielectric function, and all other interaction potentials, such as the van der Waals forces, are treated as non-electrostatic potentials. The distance dependent ion-specific free energy in excess of the purely electrostatic contribution as used in the Gouy–Chapman model is termed the potential of mean force (PMF). The PMF comprises a wide range of effects, such as the hydration potential, steric interactions, and direct interactions between the ion and the surface, which all depend on the ion's size as well as on the chemical properties of the ion and the surface. In addition, the PMF contains dielectric contributions from the oriented water molecules, which can be ion-specific, depending on the ion's size and polarizability. Finally, to satisfy the electrostatic boundary conditions for a single ion at a dielectric discontinuity, it may be necessary to consider image charge interactions. In the mean field regime, the ion distribution at finite salt concentrations can be estimated from the Poisson–Boltzmann equation by adding the PMF as a purely non-electrostatic contribution to the potential. This strategy has been successful in reproducing the most prominent ion-specific effect, the ordering of the ions into the so-called Hofmeister series.^{30–32} A more exact treatment of ion-specific effects requires splitting the PMF into its distinct contributions. Separating the PMF into contributions from the Lennard–Jones interaction, the polarizability, the image charge potential, and the electrostatic potential of the ordered water molecules, however, has not been successful up to now.³⁰ With the dielectric profile used in the present work, the dielectric part of the PMF can be properly incorporated into the Poisson equation. Because ions have little influence on the hydrogen bond structure of liquid water,³³ the dielectric profile of pure water provides a good first approximation, even at finite salt concentration.

This paper is organized as follows. First, we give an overview of the MD simulations necessary to obtain the molecular response function profiles. Second, we review the framework

for extracting the dielectric profile from the MD simulations and show the components of the dielectric tensor for water at hydrophilic and hydrophobic diamond surfaces. Third, we review the results of shear flow simulations of water between diamond surfaces and calculate the viscosity profile. Fourth, the PMFs of different ion types at uncharged self-assembled monolayers (SAMs) are shown for different atomic force fields. Fifth, we compare the results of MD simulations of Na^+ and Cl^- at diamond surfaces with the results of a Poisson–Boltzmann model, modified to incorporate the dielectric profile, as well as non-electrostatic contributions to the potential. Finally, we approximate the dielectric and hydrodynamic profiles by step functions, and calculate the double-layer capacitance, the electrokinetic mobility, and the electric conductivity at charged interfaces.

■ MOLECULAR DYNAMICS SIMULATIONS

We obtain the molecular structure of aqueous interfaces from classical molecular dynamics (MD) simulations of SPC/E water³⁴ at four different substrates, using the GROMACS simulation package.³⁵ The first two substrates are self-assembled monolayers (SAMs) consisting of single membranes of either $\text{C}_{20}\text{H}_{41}\text{OH}$ (hydrophilic, Figure 1a) or $\text{C}_{20}\text{H}_{42}$

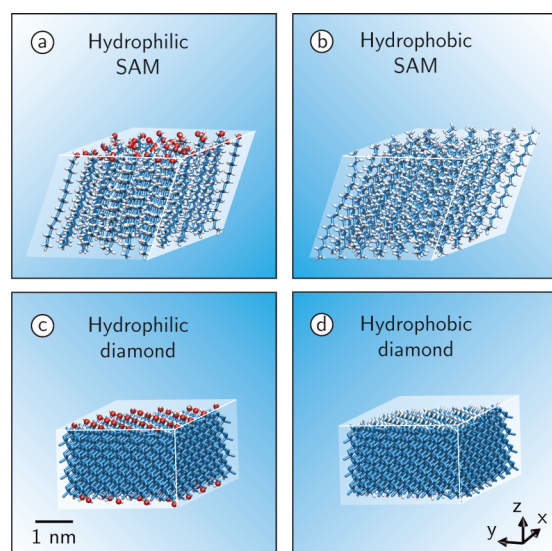


Figure 1. Simulation snapshots of (a) the hydrophilic self-assembled monolayer, (b) the hydrophobic self-assembled monolayer, (c) the hydrophilic diamond surface (OH surface coverage $x_{\text{OH}} = 1/4$), and (d) the hydrophobic diamond surface. Only the substrate in the primary simulation box is shown.

(hydrophobic, Figure 1b). The second set of substrates consists of a diamond surface (double FCC lattice of carbon atoms) with either OH termination (hydrophilic, Figure 1c) or H termination (hydrophobic, Figure 1d). The OH groups on the hydrophilic surfaces, which are free to rotate, are strongly polarized: the hydrogen atom carries a partial charge of $0.408 e$, the oxygen atom carries $-0.734 e$ (SAM) or $-0.674 e$ (diamond), and the connecting carbon atom carries $0.326 e$ (SAM) or $0.266 e$ (diamond). Further details of the simulations are described in ref 31 (SAM) and refs 24 and 27 (diamond).

At all four substrates, the water density $n(z)$ shows an oscillatory profile (Figure 2). The first peak of each profile is located closer to the surface at the hydrophilic substrates than at the hydrophobic substrates, reflecting the well-known density

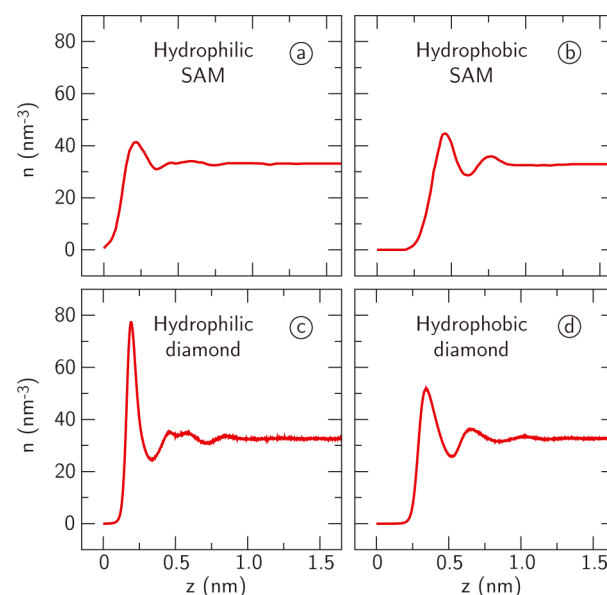


Figure 2. Number density $n(z)$ of SPC/E water molecules at the four different substrates shown in Figure 1: (a) hydrophilic (OH-terminated) self-assembled monolayer, (b) hydrophobic self-assembled monolayer, (c) hydrophilic (OH coverage $x_{\text{OH}} = 1/4$) diamond surface, and (d) hydrophobic diamond surface. The position $z = 0$ corresponds to the position of the oxygen atoms at the hydrophilic surfaces and to the position of outermost carbon atoms at the hydrophobic surfaces. The SAM profiles (a, b) are taken from ref 31.

depletion gap at hydrophobic surfaces. The water density profile at the hydrophilic diamond surface (Figure 2c) shows a significantly higher first peak than the profile at the hydrophobic surface (Figure 2d). This difference is not visible at the self-assembled monolayer due to the spatial and temporal fluctuations of the soft SAM surfaces.

■ DIELECTRIC PROFILE

To quantify the effects of the anisotropic water structure on the electrostatic properties of aqueous interfaces, we calculate all unique components of the local dielectric tensor of pure water at planar solid surfaces as a function of the coordinate normal to the interface, denoted z . As typical hydrophilic and hydrophobic substrates, we use the diamond surfaces pictured in Figure 1c and d. In previous calculations of interfacial dielectric properties, the polarization has often been estimated from the dipole density, which is exact for a fluid consisting of pure dipoles.³⁶ For water, however, higher order multipole moments play a pivotal role in water structuring and orientation,³⁷ ion solvation, the electrostatic potential difference across interfaces,³⁸ and the interfacial dielectric response.²³ Below, we summarize the formalism needed to extract the dielectric tensor from molecular coordinates, including all multipole components of the polarization. We refer to ref 24 for a more detailed treatment.

The displacement field $\vec{D}(\vec{r})$ and the electric field $\vec{E}(\vec{r})$ inside a medium are related by the nonlocal dielectric response tensor $\vec{\epsilon}_{\text{nl}}(\vec{r}, \vec{r}')$, which depends on the positions \vec{r} and \vec{r}' of source and response, with $\vec{r} = (x, y, z)$. In the linear response regime, a change in displacement field $\Delta\vec{D}(\vec{r})$ is linearly related to a change in electric field $\Delta\vec{E}(\vec{r})$ by

$$\Delta\vec{D}(\vec{r}) = \varepsilon_0 \int \vec{\varepsilon}_{\text{nl}}(\vec{r}, \vec{r}') \cdot \Delta\vec{E}(\vec{r}') d\vec{r}' \quad (2a)$$

$$\Delta\vec{E}(\vec{r}) = \varepsilon_0^{-1} \int \vec{\varepsilon}_{\text{nl}}^{-1}(\vec{r}, \vec{r}') \cdot \Delta\vec{D}(\vec{r}') d\vec{r}' \quad (2b)$$

with ε_0 being the permittivity of a vacuum. The nonlocal dielectric response function in eq 2a and its functional inverse function $\vec{\varepsilon}_{\text{nl}}^{-1}(\vec{r}, \vec{r}')$ in eq 2b satisfy the relation²²

$$\int \vec{\varepsilon}_{\text{nl}}(\vec{r}, \vec{r}') \vec{\varepsilon}_{\text{nl}}^{-1}(\vec{r}', \vec{r}'') d\vec{r}' = \delta(\vec{r} - \vec{r}'') \quad (3)$$

In case either of the fields, $\vec{E}(\vec{r})$ or $\vec{D}(\vec{r})$, is constant in space, eqs 2a and 2b can be integrated to give, respectively,

$$\Delta\vec{D}(\vec{r}) = \varepsilon_0 \vec{\varepsilon}(\vec{r}) \cdot \Delta\vec{E} \quad (4a)$$

$$\Delta\vec{E}(\vec{r}) = \varepsilon_0^{-1} \vec{\varepsilon}^{-1}(\vec{r}) \cdot \Delta\vec{D} \quad (4b)$$

with the local response functions being defined as

$$\vec{\varepsilon}(\vec{r}) = \int \vec{\varepsilon}_{\text{nl}}(\vec{r}, \vec{r}') d\vec{r}' \quad (5a)$$

$$\vec{\varepsilon}^{-1}(\vec{r}) = \int \vec{\varepsilon}_{\text{nl}}^{-1}(\vec{r}, \vec{r}') d\vec{r}' \quad (5b)$$

Note that the two response functions defined in eq 5 are disparate functions, and that they do not universally satisfy the relation $\vec{\varepsilon}(\vec{r}) \cdot \vec{\varepsilon}^{-1}(\vec{r}) = \vec{I}$. To calculate the response function from the polarization density, the electric field $\vec{E}(\vec{r})$ is expressed as the sum of the displacement field, $\vec{D}(\vec{r})$, and the polarization contribution due to the dielectric medium, $\vec{m}(\vec{r})$,

$$\varepsilon_0 \vec{E}(\vec{r}) = \vec{D}(\vec{r}) - \vec{m}(\vec{r}) \quad (6)$$

In the planar systems studied here, which have approximate translational invariance in the x and y directions, the fields $\vec{E}(\vec{r})$, $\vec{D}(\vec{r})$, and $\vec{m}(\vec{r})$ only depend on the z coordinate. In addition, the dielectric tensor has only two unique components, one parallel and one perpendicular to the interface. The expressions for the components of the dielectric tensor depend on the electrostatic boundary conditions, which we determine from Maxwell's equations $\nabla \times \vec{E}(z) = 0$ and, in absence of free charges, $\nabla \cdot \vec{D}(z) = 0$. Together with the symmetry condition that E_{\parallel} and D_{\perp} must vanish in the absence of an applied field, we arrive at the boundary conditions $\Delta E_{\parallel}(z) = E_{\parallel}$ and $\Delta D_{\perp}(z) = D_{\perp}$. Using these boundary conditions in conjunction with eqs 4 and 6 leads to expressions for both unique components of the dielectric tensor

$$\varepsilon_{\parallel}(z) = 1 + \frac{\Delta m_{\parallel}(z)}{\varepsilon_0 E_{\parallel}} \quad (7a)$$

$$\varepsilon_{\perp}^{-1}(z) = 1 - \frac{\Delta m_{\perp}(z)}{D_{\perp}} \quad (7b)$$

Applying an external field, the components of the dielectric tensor can be calculated directly from eq 7. Alternatively, the components can be calculated from the polarization fluctuations at vanishing external field strength. To this end, we write a statistical mechanical expression for the excess polarization in response to a weak, homogeneous external field \vec{F} , which corresponds to \vec{E} when applied parallel and to \vec{D}/ε_0 when applied perpendicular to the interface. Defining the total polarization by $\vec{M} = \int \vec{m}(\vec{r}) d\vec{r}$, the excess energy upon application of the external field follows as $-\vec{M} \cdot \vec{F}$. Linearizing

the ensemble average excess polarization density $\Delta\vec{m}(\vec{r})$ for small \vec{F} yields^{36,39,40}

$$\Delta\vec{m}(\vec{r}) \approx \beta [\langle \vec{m}(\vec{r}) \vec{M} \rangle_0 - \langle \vec{m}(\vec{r}) \rangle_0 \langle \vec{M} \rangle_0] \cdot \vec{F} \quad (8)$$

where $\langle \dots \rangle_0$ denotes the ensemble average without applied external field and β represents the inverse thermal energy. Inserting $F_{\parallel} = E_{\parallel}$ and $F_{\perp} = D_{\perp}/\varepsilon_0$ in eqs 7 and 8 leads to the fluctuation equations for the dielectric tensor components

$$\varepsilon_{\parallel}(z) \approx 1 + \varepsilon_0^{-1} \beta [\langle m_{\parallel}(z) M_{\parallel} \rangle_0 - \langle m_{\parallel}(z) \rangle_0 \langle M_{\parallel} \rangle_0] \quad (9a)$$

$$\varepsilon_{\perp}^{-1}(z) \approx 1 - \varepsilon_0^{-1} \beta [\langle m_{\perp}(z) M_{\perp} \rangle_0 - \langle m_{\perp}(z) \rangle_0 \langle M_{\perp} \rangle_0] \quad (9b)$$

The polarization density $\vec{m}(z)$ needed to evaluate eqs 7 and 9 is calculated from the atomic charge distribution in the molecular dynamics simulation trajectory in two different ways.

In the first method, the polarization is determined by integrating the charge density. To calculate the parallel polarization density, we introduce a virtual cut perpendicular to the x axis, splitting some water molecules into their charged components. Cutting the water molecules this way creates a virtual monopole charge density $\pm P_0(x, z)$ on either side of the cut. In the y direction, the system is still spatially invariant. Now we carve out a volume \mathcal{V} by closing the surface of the cut without splitting any other water molecules, so that the x dependence of $P_0(x, z)$ has the shape of a delta peak at the position of the cut. The integral in the x direction of the virtual monopole density over the volume \mathcal{V} resembles a surface charge density which is only nonzero at the position of the virtual cut, and which equals the projection of the polarization density onto the surface normal \hat{n} of the cut

$$\int_{\mathcal{V}} P_0(x, z) dx = -\vec{m}(z) \cdot \hat{n} \quad (10)$$

Since the virtual cut is perpendicular to the x axis, it follows that $\vec{m}(z) \cdot \hat{n} = \pm m_{\parallel}(z)$. With eq 10, we find

$$m_{\parallel}(z) = \mp \int_{\mathcal{V}} P_0(x, z) dx \quad (11a)$$

where the different signs apply to closing the volume \mathcal{V} and integrating $P_0(x, z)$ on the different sides of the cut. For more details, see ref 24.

The perpendicular polarization density is calculated from an integral in the z direction over the total charge density

$$m_{\perp}(z) = - \int_0^z \rho(z') dz' \quad (11b)$$

The total charge density $\rho(z)$ in eq 11b is given by the sum over all point charges q_j^i associated with all atoms $j(i)$ of all molecules i

$$\rho(\vec{r}) = \sum_i \sum_{j(i)} q_j^i \delta(\vec{r} - \vec{r}_j^i) \quad (12)$$

with \vec{r}_j^i being the atomic positions.

The second method to calculate $\vec{m}(z)$ is to expand the polarization density further into its separate multipole contributions

$$\vec{m}(\vec{r}) = \vec{P}_1(\vec{r}) - \nabla \cdot \vec{P}_2(\vec{r}) + \nabla \nabla : \vec{P}_3(\vec{r}) - \dots \quad (13)$$

with \vec{P}_1 being the dipole moment per unit volume, \vec{P}_2 the quadrupole moment, \vec{P}_3 the octupole moment, etc. The individual multipole moments are calculated directly from the

distribution of partial charges q_j^i on the atoms $j(i)$ of the water molecules i (the “bound” charge density). The multipole density of order $l \in \{0, 1, 2, \dots\}$ is given by a summation over all molecules i

$$\vec{P}_l(\vec{r}) = \sum_i \vec{p}_{li} \delta(\vec{r} - \vec{r}_i) \quad (14)$$

with \vec{r}_i being an arbitrary point within each molecule. The molecular multipole moment \vec{p}_{li} of order l is found by summing over all atoms $j(i)$ of the molecule

$$\vec{p}_{li} = \frac{1}{l!} \sum_{j(i)} q_j^i (\vec{r}_j^i - \vec{r}_i)^l \quad (15)$$

where the power denotes serial direct vector multiplication. Whereas eqs 11a and 11b implicitly include all moments of the charge distribution, the sum in eq 13 is truncated after a finite number of terms.

With eqs 7 and 9 for the response function and eqs 11 and 13 for the polarization density, we have a total of four different methods to calculate the dielectric tensor. For both unique components of the dielectric tensor at hydrophilic and hydrophobic diamond surfaces, the results of all four methods coincide, as expected (Figure 3). The parallel component of the dielectric tensor $\epsilon_{\parallel}(z)$ (Figure 3a,b) exhibits a profile that is similar in shape to the molecular density profile (Figure 2c,d). There are subtle differences, however, between the two surface types. Whereas the first peak of $\epsilon_{\parallel}(z)$ is lower at the hydrophilic surface than at the hydrophobic surface, the peak heights of the density profiles follow the inverse sequence. This difference in peak heights reveals a significant difference in interfacial water structure between hydrophilic and hydrophobic surfaces, that we will get back to in the context of the dielectric dividing surface further below. The perpendicular component of the inverse dielectric tensor $\epsilon_{\perp}^{-1}(z)$ shows completely different behavior, oscillating strongly and passing through zero several times (Figure 3c,d). The negative regions in the dielectric response function are an indication of overscreening. For the analogous system of electrolytes at charged surfaces, that would correspond to the situation where the co-ion concentration locally exceeds the counterion concentration, a phenomenon that has attracted attention previously in the context of ionic liquids.⁴¹

To study the differences between the dielectric properties at hydrophilic and hydrophobic surfaces quantitatively, we extract a single length scale that we call the dielectric dividing surface position z_{DDS}^{23}

$$z_{\parallel}^{\text{DDS}} = z_v + \int_{z_v}^{z_l} \frac{\epsilon_{\parallel}(z_l) - \epsilon_{\parallel}(z)}{\epsilon_{\parallel}(z_l) - \epsilon_{\parallel}(z_v)} dz \quad (16a)$$

$$z_{\perp}^{\text{DDS}} = z_v + \int_{z_v}^{z_l} \frac{\epsilon_{\perp}^{-1}(z_l) - \epsilon_{\perp}^{-1}(z)}{\epsilon_{\perp}^{-1}(z_l) - \epsilon_{\perp}^{-1}(z_v)} dz \quad (16b)$$

with z_v and z_l being positions far away from the interface, in the substrate and the bulk liquid, respectively. The dielectric dividing surface is the analogue of the Gibbs dividing surface, which is defined using the number density of water $n(z)$

$$z^{\text{GDS}} = z_v + \int_{z_v}^{z_l} \frac{n(z_l) - n(z)}{n(z_l) - n(z_v)} dz \quad (17)$$

The numerical values of $z_{\parallel}^{\text{DDS}}$, z_{\perp}^{DDS} , and z^{GDS} at the hydrophilic and hydrophobic diamond surfaces are summarized in Table 1.

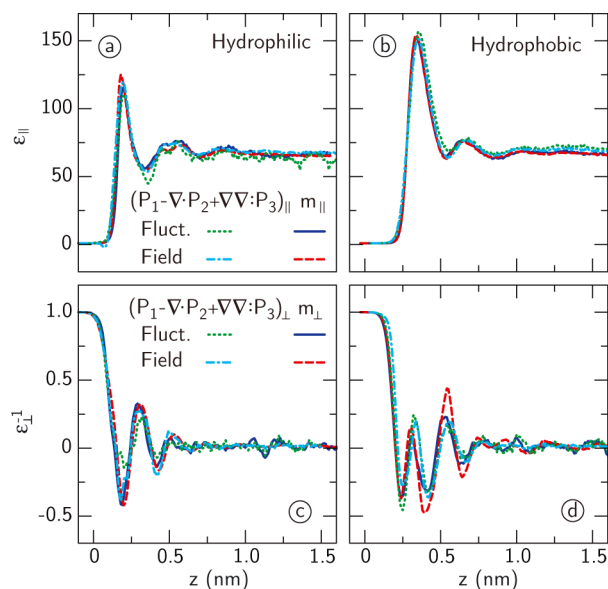


Figure 3. Top: Parallel dielectric function $\epsilon_{\parallel}(z)$ next to (a) the hydrophilic and (b) the hydrophobic diamond, calculated from the total polarization $m_{\parallel}(z)$ (eq 11a) and from an explicit expansion of the polarization up to the octupole term (eq 13). The response is calculated in two different ways: from the excess polarization $\Delta m_{\parallel}(z)$ resulting from an applied external electric field in parallel direction of $E_{\parallel} = 0.05$ V/nm (eq 7a) and from polarization fluctuations at vanishing external field (eq 9a). Bottom: Inverse perpendicular dielectric function $\epsilon_{\perp}^{-1}(z)$ next to (c) the hydrophilic and (d) the hydrophobic diamond, calculated from the total polarization $m_{\perp}(z)$ (eq 11b) and from an explicit expansion of the polarization up to the octupole term (eq 13). The response is calculated in two different ways: from the excess polarization $\Delta m_{\perp}(z)$ resulting from an applied external displacement field in perpendicular direction (eq 7b) and from polarization fluctuations (eq 9b). For the curves corresponding to the total polarization $\Delta m_{\perp}(z)$, the applied field is $D_{\perp}/\epsilon_0 = 0.5$ V/nm. The curves corresponding to the explicit expansion (dashed-dotted lines) have been averaged over applied field strengths of $D_{\perp}/\epsilon_0 = 2.0, 4.0$, and 8.0 V/nm. All four different methods give comparable results.

Table 1. Dielectric and Gibbs Dividing Surface Positions (eqs 16 and 17) at the Two Different Diamond Surface Types^a

surface type	z^{GDS} (nm)	$z_{\parallel}^{\text{DDS}}$ (nm)	z_{\perp}^{DDS} (nm)
hydrophilic	0.07	0.09	0.10
hydrophobic	0.22	0.08	0.12

^aMeasured with respect to the laterally averaged position of the outermost heavy atoms, i.e., the oxygen atoms of the hydroxyl group at the hydrophilic surface and the carbon atoms at the hydrophobic surface

Interestingly, the differences between z_{\perp}^{DDS} and $z_{\parallel}^{\text{DDS}}$ at hydrophilic and hydrophobic interfaces are minor compared to the difference between z^{GDS} , indicating an important difference in interfacial water structure between the two surface types.^{23,24,42} Broadly speaking, the water at hydrophobic surfaces is more polarizable, compensating for the decreased water density (as reflected by the large value of z^{GDS}) and leading to a dielectric dividing surface position similar to the one at the hydrophilic surface. Further below, we will use the dielectric dividing surface to construct a simplified model of the interfacial dielectric properties.

VISCOSITY PROFILE

For large-scale fluid flow along a solid boundary, it is well-established that the velocity profile typically obeys the so-called no-slip boundary condition, i.e., the condition that the fluid velocity relative to the boundary vanishes at the boundary. At small length scales, however, the hydrodynamic boundary condition for tangential flow along solid surfaces often deviates from the no-slip boundary condition, which is important for fluid flow through small channels.²⁸

Two fundamentally different scenarios occur in nature. At hydrophobic surfaces, the solid and the fluid are separated by a depletion gap, which decreases friction and gives rise to a nonzero fluid velocity at the interface,^{43–45} a phenomenon that is generally referred to as slip. The most common way to describe tangential slip at a solid surface is by imposing proportionality between the rate of strain and the tangential fluid velocity $u_{\parallel}(z)$ at the shear plane. With the fluid occupying the space $z > 0$ and the shear plane located at $z = 0$, the boundary condition reads

$$b \nabla u_{\parallel}(z)|_{z=0} = u_{\parallel}(0) \quad (18)$$

In eq 18, the length scale b is called the slip length. The hydrophobicity of the surface can be characterized by the contact angle of a water droplet on the surface, which ranges from 0° at very hydrophilic substrates to 180° for extremely hydrophobic substrates. Both the width of the depletion gap and the slip length increase strongly with increasing contact angle.²⁷ Equation 18, which is referred to as the Navier boundary condition, can be used to describe the velocity profile of the fluid at hydrophobic surfaces down to the depletion gap. At hydrophilic surfaces, on the other hand, no depletion gap exists. At the same time, the viscosity in the first few water layers at the wall is higher than that in bulk.^{27,46} The flow profile far away from the interface can be modeled using eq 18 with a negative slip length b , corresponding to the width of a stagnant layer of fluid sticking to the surface in a Couette shear flow experiment. Whereas a positive slip length greatly enhances flow rates, a stagnant layer hinders flow through small capillaries. As an alternative to using eq 18, the effect of the interfacial hydrodynamics can be modeled by a space-dependent viscosity profile $\eta(z)$. Although the exact meaning of a viscosity profile which varies at subatomic length scales is debatable, such a viscosity profile can be used in a continuum model to reproduce flow characteristics found experimentally at large distances from the surface. Whether a slip length, a viscosity profile, or a combination of the two provides the more appropriate model of the hydrodynamic boundary condition depends on surface type and molecular composition.

Viscosity profiles are calculated from molecular dynamics simulations of an SPC/E water slab confined between two diamond surfaces.²⁷ To the two diamond surfaces, forces F_0 and $-F_0$ are applied to create a shear profile in the fluid. The resulting velocity profiles $u_{\parallel}(z)$, normalized on the force per unit area F_0/\mathcal{A} , are shown in Figure 4 for (a) the hydrophilic ($x_{\text{OH}} = 1/4$) and (b) the hydrophobic diamond surface displayed in Figure 1c,d. The velocity of the left-hand surface ($z = 0$) is set to zero. The expected velocity profile when $\eta(z) = \eta_{\text{bulk}}$ is shown in both panels as a dashed line, with the bulk viscosity $\eta_{\text{bulk}} = 0.642 \text{ mPa}\cdot\text{s}$ of SPC/E water.⁴⁷ At the hydrophilic surface, the velocity at the wall starts at $u_{\parallel}(z) = 0$ and initially increases slower than expected for $\eta(z) = \eta_{\text{bulk}}$. At the hydrophobic surface on the other hand, the fluid slips along

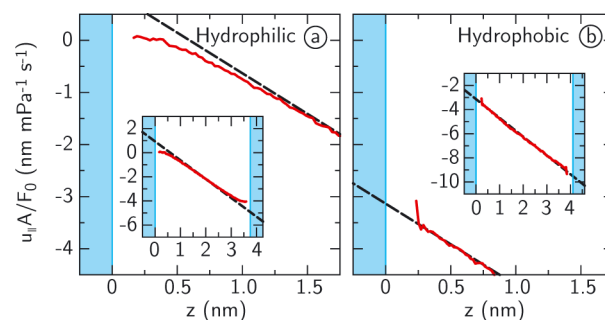


Figure 4. Normalized velocity profile $u_{\parallel}\mathcal{A}/F_0$ resulting from application of forces $\pm F_0$ to the (a) hydrophilic and (b) hydrophobic diamond with surface area \mathcal{A} . The hydrophilic diamond has an OH-coverage of $x_{\text{OH}} = 1/4$ in the notation of ref 27. The position $z = 0$ corresponds to the oxygen layer of the hydroxyl groups (hydrophilic surface) or the outermost carbon layer (hydrophobic surface) of the left-hand surface, of which the velocity is set to zero. Dashed lines indicate the expected velocity profile if $\eta(z) = \eta_{\text{bulk}}$. The velocity profiles across the full width of the channel are shown in the insets. The data shown in panel a are taken from ref 27.

the wall, but the rate at which the velocity increases follows the prediction for bulk viscosity for $z \gtrsim 0.25 \text{ nm}$. From Cauchy's stress principle, it follows

$$-\frac{F_0}{\mathcal{A}} = \Pi_{zx} = \Pi_{zy} = \eta(z) \nabla_z u_{\parallel}(z) \quad (19)$$

with $\eta(z)$ being the viscosity profile, \mathcal{A} the surface area of the diamond, Π the stress tensor of the fluid, and $\pm F_0$ the applied force. In Figure 5, we show $\eta(z)$ at (a) the hydrophilic diamond

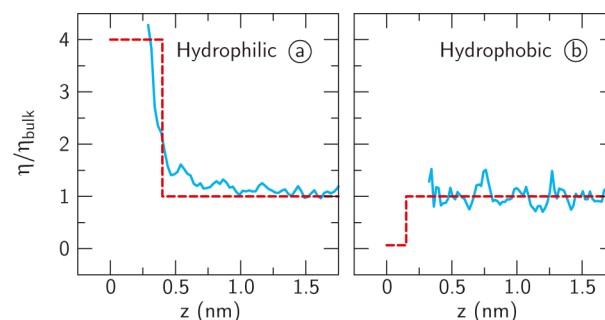


Figure 5. Viscosity profiles $\eta(z)/\eta_{\text{bulk}}$ at (a) the hydrophilic and (b) the hydrophobic diamond surface, calculated from eq 19 (blue solid lines). The profiles are normalized on the bulk viscosity of SPC/E water, $\eta_{\text{bulk}} = 0.642 \text{ mPa}\cdot\text{s}$. Red dashed lines denote the step function approximation of eq 32 with the parameters $\eta_i = 4\eta_{\text{bulk}}$ and $z_s = 0.4 \text{ nm}$ (hydrophilic) and $\eta_i = \eta_{\text{bulk}}/15$ and $z_s = 0.15 \text{ nm}$ (hydrophobic).

surface and (b) the hydrophobic diamond surface, calculated from the velocity profiles shown in Figure 4 using eq 19. The viscosity profiles are normalized on the bulk viscosity η_{bulk} . Clearly, the viscosity increases steeply at the hydrophilic surface, whereas it remains constant at the hydrophobic surface down to the depletion gap. At both surface types, the simulated viscosity profiles agree with experimental results⁴⁸ and previous simulations.^{26,27} Although flow profiles at hydrophilic interfaces can be successfully modeled using a single effectively stagnant layer of water molecules ($\sim 0.3 \text{ nm}$),^{49,50} the length scale at which the viscosity at the hydrophilic surface reaches the bulk value is remarkably large, spanning about three layers of water molecules. Further below, we introduce an unambiguous

mapping of $\eta(z)$ onto approximate square-well profiles which are suitable for further analytic modeling.

IONIC POTENTIALS OF MEAN FORCE

The free energy of interaction between a single ion and a surface can be extracted from MD simulations using umbrella sampling, in which a restraining potential is used to sample the free energy landscape as a function of the distance from the interface.⁵¹ At uncharged surfaces, the resulting energy landscape includes contributions from the Lennard-Jones potential and the atomic polarizability, as well as electrostatic contributions due to water orientation. In addition, single ions at a surface are subject to image charge interactions due to the dielectric boundary. The total free energy, termed the potential of mean force (PMF), depends sensitively on surface type and ion type, as well as on the force field used to parametrize the ion. Polarizable ions (Figure 6a) are adsorbed more easily than

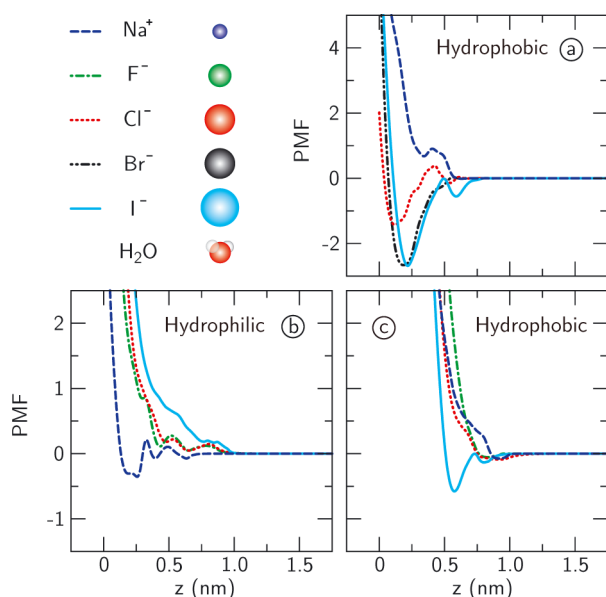


Figure 6. Potentials of mean force (PMFs) for ions at hydrophilic and hydrophobic SAMs, using (a) polarizable and (b–c) non-polarizable force fields. Data is taken from (a) refs 30 and 51 and (b, c) ref 31. The radii of the spheres shown in the top left panel are proportional to the Lennard-Jones size λ_{LJ} of the ions. A water molecule is shown for comparison.

non-polarizable ions (Figure 6b,c), and also reside closer to the interface. Note, however, that the Lennard-Jones interaction parameters are equally important for determining the ion-surface affinity; see ref 52 for a detailed discussion. The different surface affinities can be at least partly explained by considering the repulsive image charge interactions, which are more pronounced for non-polarizable ions.^{42,53} For both polarizable and non-polarizable force fields, big ions are adsorbed onto hydrophobic surfaces (Figure 6a and c). On the other hand, big ions are not adsorbed onto hydrophilic surfaces (Figure 6b). A small ion like sodium is adsorbed onto hydrophilic surfaces (Figure 6b) but not onto hydrophobic ones (Figure 6a and c). In the following sections, we identify the physical mechanisms responsible for these qualitative differences by considering the separate factors contributing to the PMF. Note that, although the non-polarizable atomic force fields employed in Figure 6b,c are adequate to model

monatomic ions, force fields for large, multiatomic ions such as IO_3^- and NO_3^- have many more degrees of freedom, and their behavior does not necessarily follow the same patterns.

MODIFIED CONTINUUM EQUATIONS

In order to use the results of the molecular simulations presented in the preceding sections to calculate experimentally measurable quantities, we incorporate the molecular profiles into a continuum description. At infinite dilution, the probability distribution of the ion density scales with the Boltzmann factor of the PMF. Ion densities at finite salt concentrations can be estimated by using the Gouy–Chapman theory to calculate the electrostatic interactions, and adding the PMF as a purely non-electrostatic contribution to the potential.⁵¹ A more precise treatment, however, requires treating the part of the PMF that is due to the ordered water molecules using the dielectric function shown in Figure 3. In this work, we incorporate the dielectric profile into the continuum equations at different levels of approximation, as will be explained below. The remaining part of the PMF is either estimated from the shape and length scale of the Lennard-Jones interaction potential or taken into account by a heuristic function.

Our model consists of a smooth surface carrying a homogeneous surface charge density σ_0 , extending infinitely in lateral direction, in contact with an electrolyte with ionic charge density $P_0(z)$. The ions are modeled as point charges, subject to the electrostatic mean-field potential and an ion-specific non-electrostatic term $\mu_{\pm}(z)$. Image charge interactions, which form part of the potential of mean force for a single ion, do not appear in the mean-field potential because the electrostatic boundary conditions at the interface are satisfied explicitly by the extended Poisson–Boltzmann equation. In a system with a nonzero monopole density, eq 4b is not strictly valid. Therefore, we need the assumption that the electric field is linearly related to the displacement field by the local inverse dielectric tensor $\epsilon_{\perp}^{-1}(z)$

$$\epsilon_0 E_{\perp}(z) = \epsilon_{\perp}^{-1}(z) D_{\perp}(z) \quad (20)$$

Taking the derivative of eq 20 and using $\nabla\psi(z) = -E_{\perp}(z)$, with $\psi(z)$ being the electrostatic potential, and $\nabla D_{\perp}(z) = P_0(z)$, with $P_0(z)$ being the ionic charge density, we arrive at the extended Poisson equation

$$\epsilon_0 \nabla^2 \psi(z) = -\epsilon_{\perp}^{-1}(z) P_0(z) - D_{\perp}(z) \nabla \epsilon_{\perp}^{-1}(z) \quad (21)$$

Up to an integration constant, the displacement field $D_{\perp}(z)$ is given by

$$D_{\perp}(z) = \int_0^z P_0(z') dz' \quad (22)$$

Equations 21 and 22 constitute an integro-differential equation.⁵⁴ For a solution of monovalent ions, the free charge density is calculated from the ionic densities $c_+(z)$ and $c_-(z)$

$$P_0(z) = e(c_+(z) - c_-(z)) \quad (23)$$

with e being the absolute charge of an electron. To ensure that the ionic density does not exceed its physical limit set by the ionic volume, we include a fermionic steric interaction to calculate the ion density profiles from the unrestricted ionic densities $\tilde{c}_+(z)$ and $\tilde{c}_-(z)$ ^{55–59}

$$c_{\pm}(z) = \frac{\sqrt{2}\tilde{c}_{\pm}(z)}{\sqrt{2} + \lambda_{+}^3(\tilde{c}_{+}(z) - c_0) + \lambda_{-}^3(\tilde{c}_{-}(z) - c_0)} \quad (24)$$

with c_0 being the bulk salt concentration and λ_{+} and λ_{-} the diameters of positive and negative ions, respectively. The denominator in eq 24 restricts the maximum density $c_{\pm}(z)$ to $(2)^{1/2}\lambda_{\pm}^{-3}$, which is the maximum density of close-packed (face-centered cubic or hexagonal close-packed) spheres of diameter λ_{\pm} . Because we consider relatively small ions, either at low salt concentration or at vanishing surface charge density, the steric interaction does not affect the calculations presented in this work.⁶⁰ The unrestricted ionic densities $\tilde{c}_{+}(z)$ and $\tilde{c}_{-}(z)$ follow the Boltzmann distribution

$$\tilde{c}_{\pm}(z) = c_0 \exp(-\mu_{\pm}(z) \mp \beta e\psi(z)) \quad (25)$$

with β being the inverse thermal energy and $\mu_{+}(z)$ and $\mu_{-}(z)$ the non-electrostatic contributions to the potential of the positive and negative ions, respectively. Combining eqs 21, 22, 23, 24, and 25 yields the extended Poisson–Boltzmann equation that we will use in the following sections. Apart from the approximations inherent to mean field theory,⁶¹ our extended Poisson–Boltzmann equation is based on the approximation of eq 20. Equation 20 is valid for a slowly varying $D_{\perp}(z)$, corresponding to a low surface charge density or low salt concentration.^{22,23}

In MD simulations, the non-electrostatic interaction potential $\mu_{\pm}(z)$ contains all contributions from the Lennard-Jones interaction energy. Although the Lennard-Jones potential between each pair of atoms includes an attractive term, the total Lennard-Jones interaction between an ion and a surface is repulsive.⁵¹ We approximate the non-electrostatic interaction between the ion and the surface by a hard-wall repulsion, convoluted with a spherical volume of radius λ_{LJ} , as is adequate for the repulsive interaction between a spherically symmetric particle and a planar wall. For the length scale of the repulsion, we take the Lennard-Jones interaction parameter λ_{LJ} , which defines the distance at which the Lennard-Jones interaction potential turns repulsive. Defining the distance from the hard wall as $z' = z - z_0$, the interaction potential with the wall is given by

$$\mu_{\pm}^{\text{w}}(z') = B \begin{cases} 1 & \text{if } z' < -\lambda_{\text{LJ}} \\ \frac{(2\lambda_{\text{LJ}} + z')(\lambda_{\text{LJ}} - z')^2}{4\lambda_{\text{LJ}}^3} & \text{if } |z'| < \lambda_{\text{LJ}} \\ 0 & \text{if } z' > \lambda_{\text{LJ}} \end{cases} \quad (26)$$

Because the volume density of hydroxide groups at the hydrophilic surface is very low, the position z_0 of the hard wall is chosen to be the position of the outermost carbon atom: $z_0 = -0.11$ nm at hydrophilic surfaces and $z_0 = 0$ at hydrophobic surfaces. For the radius λ_{LJ} , we use the Lennard-Jones radius of the ion–carbon interaction ($\lambda_{\text{LJ}} = 0.282$ nm for Na^{+} and $\lambda_{\text{LJ}} = 0.402$ nm for Cl^{-} ⁶²). The strength B of the repulsion is treated as a fit parameter. The ions also experience solvation repulsion from the water phase, which is proportional to the immersed volume of the ions. Similar to eq 26, this hydration interaction potential is given by the convolution of the ionic volume with a step function located at the Gibbs dividing surface z^{GDS}

$$\mu_{\pm}^{\text{h}}(z'') = -\frac{4\pi\lambda_{\text{h}}^3 C}{3} \begin{cases} 1 & \text{if } z'' < -\lambda_{\text{h}} \\ \frac{(2\lambda_{\text{h}} + z'')(\lambda_{\text{h}} - z'')^2}{4\lambda_{\text{h}}^3} & \text{if } |z''| < \lambda_{\text{h}} \\ 0 & \text{if } z'' > \lambda_{\text{h}} \end{cases} \quad (27)$$

with $z'' = z - z^{\text{GDS}}$. The magnitude of the hydration energy is calculated from the solvation of hard spheres, giving values in the range of $\beta C = 68 \text{ nm}^{-3}$ ⁶³ and $\beta C = 78 \text{ nm}^{-3}$,⁵² with β being the inverse thermal energy. The length scale of the hydration interaction has been estimated in MD simulations to be $\lambda_{\text{h}} = 0.224$ nm for Na^{+} and $\lambda_{\text{h}} = 0.298$ nm for Cl^{-} .⁶⁴

In the following sections, we use different levels of approximation to reproduce both the ion density profiles at charged surfaces calculated using atomistic MD simulations and experimental results for the static and kinetic properties of charged substrates in water. The different approximations used are summarized in Table 2: (I) the Gouy–Chapman model;

Table 2. Different Levels of Approximation Used for the Dielectric Profile $\epsilon_{\perp}^{-1}(z)$, the Viscosity $\eta(z)$, the Non-Electrostatic Interaction $\mu_{\pm}(z)$, and the Electrophoretic Mobility $\nu_{\pm}(z)$ ^a

model	$\epsilon_{\perp}^{-1}(z)$	$\eta(z)$	$\mu_{\pm}(z)$	$\nu_{\pm}(z)$	description
I	$\epsilon_{\text{bulk}}^{-1}$	η_{bulk}	0	ν	Gouy–Chapman
II	$\epsilon_{\text{bulk}}^{-1}$		Figure 6		PMF
III	eq 28	Figure 5	eqs 26 and 27	eq 43	full profiles
IV	eq 31	eq 32	eq 35	eq 34	step functions

^aThe figure and equation numbers refer to the equations where the functions are defined or the figures where the profiles are shown.

(II) numerical solutions to the extended Poisson–Boltzmann equation using the PMF; (III) static solutions using the dielectric profile and a non-electrostatic contribution to the ionic free energy in the extended Poisson–Boltzmann equation, and dynamic solutions using the viscosity profile and the electrophoretic mobility profile in the generalized hydrodynamic equations; and (IV) static and dynamic solutions using step-function approximations for the molecular profiles.

ION DENSITY PROFILES

We solve the extended Poisson–Boltzmann equation (eqs 21–25) to calculate the ionic density profiles $c_{\pm}(z)$ for Na^{+} and Cl^{-} at the hydrophilic and hydrophobic diamond surfaces shown in Figure 1c and d and compare the profiles to the results from MD simulations. The surfaces carry a homogeneous surface charge density σ_0 , and we use the boundary conditions $\lim_{z \rightarrow \infty} \psi(z) = 0$ and overall charge neutrality.

The PMFs shown in Figure 6 include all contributions to the free energy of a single ion at an uncharged SAM. Assuming that a moderate surface charge density does not affect the electrostatic part of the PMF much, we solve the extended Poisson–Boltzmann equation with $\mu_{\pm}(z)$ equal to the PMF, setting $\epsilon_{\perp}^{-1}(z) = \epsilon_{\text{bulk}}^{-1}$ (model II in Table 2). In Figure 7, the results are shown for non-polarizable ions with bulk concentration $c_0 = 1$ mM at SAMs with surface charge densities $\sigma_0 = \pm 0.3 \text{ e nm}^{-2}$, using the different signs for negative and positive counterions, respectively. The smallest ion, Na^{+} , is adsorbed onto the hydrophilic surface more strongly than predicted by the Gouy–Chapman theory (model I in Table 2),

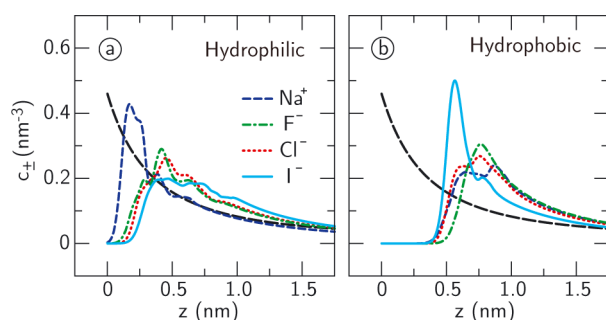


Figure 7. Density profiles for different types of counterions at (a) hydrophilic and (b) hydrophobic charged self-assembled monolayers, calculated from eqs 21–25, using the PMFs from the non-polarizable force fields (Figure 6b,c) for $\mu_{\pm}(z)$ and $\epsilon_{\perp}^{-1}(z) = \epsilon_{\text{bulk}}^{-1}$ (model II in Table 2). The profiles are calculated at a bulk salt concentration of $c_0 = 1$ mM and a bare surface charge density of $\sigma_0 = 0.3$ e/nm² for the anions and $\sigma_0 = -0.3$ e/nm² for Na⁺. Co-ion densities are not shown because they are negligible at this salt concentration. Predictions of the Gouy–Chapman theory are shown as black dashed lines (model I in Table 2).

the latter of which is shown as black dashed lines. At the hydrophobic surface, on the other hand, only the biggest ion, I[−], shows significant affinity for the surface, which we ascribe to the contribution from the hydration energy embodied in the PMF shown in Figure 6. All ions treated here accumulate closer to the hydrophilic surface than to the hydrophobic surface.

To check the results of these coarse grained calculations, we perform simulations of Cl[−] and Na⁺ with explicit solvent at hydrophilic and hydrophobic diamond surfaces (depicted in Figure 1c,d), carrying surface charge densities σ_0 on the layer of oxygen atoms (hydrophilic surface) or outermost carbon atoms (hydrophobic surface). Like the calculations described above, the simulations are performed in the limit of low salt concentration, where only counterions are present in the simulation box. The simulation box is $3.2 \times 3.2 \times 8.8$ nm³, containing 2308 SPC/E water molecules and 6 or 12 counterions. Simulations are run for 150 or 100 ns, at $\sigma_0 = \pm 0.3$ e nm^{−2} and $\sigma_0 = \pm 0.6$ e nm^{−2}, respectively. The ionic force fields we use are optimized with respect to the ionic solvation free energy, leading to Lennard-Jones parameters $\lambda_{\text{LJ}} = 0.222$ nm, $\epsilon_{\text{LJ}} = 1.54$ kJ mol^{−1} (Na⁺) and $\lambda_{\text{LJ}} = 0.452$ nm, $\epsilon_{\text{LJ}} = 0.420$ kJ mol^{−1} (Cl[−]), using geometric combination rules.⁶² Qualitatively, the simulated profiles at the diamond surfaces (blue solid lines in Figures 8 and 9) show the same behavior as the profiles at the SAMs (Figure 7), calculated using the PMFs (model II in Table 2): Whereas Na⁺ exhibits a peak at hydrophilic surfaces and not at hydrophobic surfaces, Cl[−] shows the opposite trend. At the diamond surfaces, however, the peaks are more pronounced than at the SAMs, because the rigid substrates limit the effect of thermal averaging.

In the remainder of this section, we reconstruct the simulated ion density profiles at the diamond surfaces using the dielectric profile and a non-electrostatic contribution to the free energy. The model presented here is aimed at capturing the basic features of the PMF of monatomic ions, using ion size as the only ion-specific parameter. To capture all aspects of ion specificity, especially for multiautomic ions, more complex models are needed. In the linear response regime, non-polarizable ions in in-homogeneous dielectrics can be treated as point charges in an effective dielectric profile given by the convolution of the dielectric profile with the normalized surface

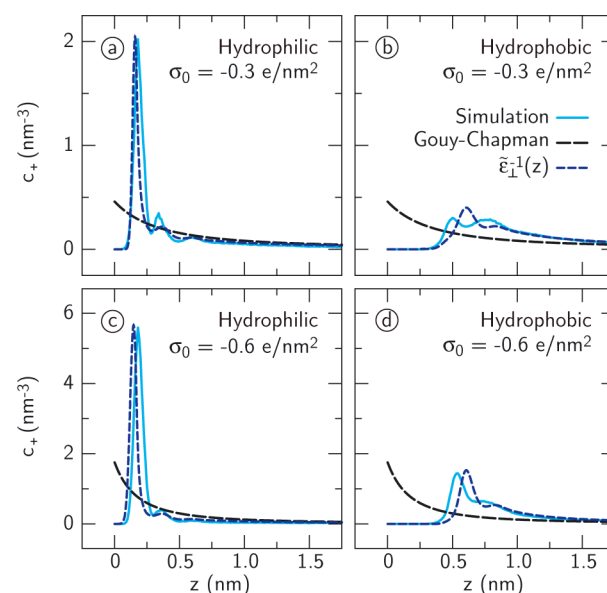


Figure 8. Density of sodium ions at (a and c) hydrophilic and (b and d) hydrophobic diamond surfaces with a surface charge density of (a and b) $\sigma_0 = -0.3$ e nm^{−2} and (c and d) $\sigma_0 = -0.6$ e nm^{−2}. Blue solid lines denote the density from simulations, and black dashed lines denote the Gouy–Chapman approximation (model I in Table 2: $\epsilon_{\perp}^{-1}(z) = \epsilon_{\text{bulk}}^{-1}$). Blue dashed lines denote the density profile using model III in Table 2: the dielectric profile $\tilde{\epsilon}_{\perp}^{-1}(z)$ (eq 28) represents the convolution of $\epsilon_{\perp}^{-1}(z)$ at an uncharged surface with the normalized surface area of an ion of diameter $\lambda_d = 0.330$ nm (eq 29) and $\mu_+(z) = \mu_+^w(z)$ (eq 26) with $\lambda_{\text{LJ}} = 0.282$ nm and $z_0 = -0.11$ nm at the hydrophilic surface and $z_0 = 0$ nm at the hydrophobic surface.

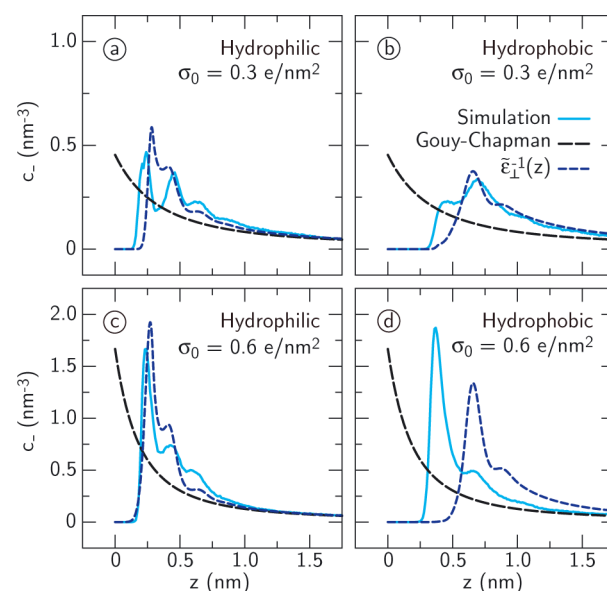


Figure 9. Density of chloride ions at (a and c) hydrophilic and (b and d) hydrophobic diamond surfaces with a surface charge density of (a and b) $\sigma_0 = 0.3$ e nm^{−2} and (c and d) $\sigma_0 = 0.6$ e nm^{−2}. Blue solid lines denote the density from simulations, and black dashed lines denote the Gouy–Chapman approximation (model I in Table 2: $\epsilon_{\perp}^{-1}(z) = \epsilon_{\text{bulk}}^{-1}$). Blue dashed lines denote the density profile using model III in Table 2: $\tilde{\epsilon}_{\perp}^{-1}(z)$ (eq 28), representing the convolution of the dielectric profile $\epsilon_{\perp}^{-1}(z)$ at an uncharged surface with the normalized surface area of an ion of diameter $\lambda_d = 0.446$ nm (eq 29) and $\mu_-(z) = \mu_-^w(z)$ (eq 26 with $\lambda_{\text{LJ}} = 0.402$ nm and $z_0 = -0.11$ nm and $z_0 = 0$ nm at hydrophilic and hydrophobic surfaces, respectively).

area of the ion.⁶⁵ Accordingly, we convolute the dielectric profiles $\epsilon_{\perp}^{-1}(z)$ shown in Figure 3c,d with the normalized surface area of a sphere of diameter λ_d

$$\tilde{\epsilon}_{\perp}^{-1}(z) = \int \epsilon_{\perp}^{-1}(z') s(z - z') dz' \quad (28)$$

with the normalized atomic surface area density being given by

$$s(z) = \begin{cases} \frac{1}{\lambda_d} & \text{if } |z| < \frac{\lambda_d}{2} \\ 0 & \text{otherwise} \end{cases} \quad (29)$$

Convolution according to eqs 28 and 29 is identical to calculating a running average over λ_d . The dielectric diameter λ_d is estimated from the ionic solvation free energy ΔG as^{24,42}

$$\lambda_d = \frac{e^2(1 - \epsilon_{\text{bulk}})}{4\pi\epsilon_0\epsilon_{\text{bulk}}\Delta G} \quad (30)$$

Using the solvation free energy ΔG with respect to which the MD force fields are optimized,⁶² we find $\lambda_d = 0.446$ nm for Cl^- and $\lambda_d = 0.330$ nm for Na^+ .

Apart from high positive electric fields at hydrophobic surfaces, external electric fields do not affect the dielectric profile much.²⁴ Therefore, despite the electric field between the surface and the first peak of ions being as high as ± 10 V/nm at $\sigma_0 = \pm 0.6$ e nm⁻², we use the dielectric profile determined at zero external electric field. To keep the model as simple as possible, we first use $\mu_{\pm}(z) = \mu_{\pm}^w(z)$ from eq 26, because the repulsive ion–wall interaction $\mu_{\pm}^w(z)$ dominates the non-electrostatic part of the free energy. Above a threshold of $B \approx 100$, the solution for $c_{\pm}(z)$ appears to be relatively insensitive to the non-electrostatic interaction strength B ; for our calculations, we use $B = 200$.

Figure 8 shows a comparison between the density of Na^+ at negatively charged surfaces from MD simulations with explicit water (blue solid lines), using Gouy–Chapman theory (model I in Table 2, black dashed lines), and the solution to the extended Poisson–Boltzmann equation (model III, blue dashed lines). Clearly, the Gouy–Chapman theory fails to describe the profiles from the simulations, whereas the extended Poisson–Boltzmann equation captures the simulated profiles with remarkable accuracy. In particular, the strong adsorption of Na^+ onto hydrophilic surfaces (Figure 8a,c) but not onto hydrophobic surfaces (Figure 8b,d)—which is seen in the density profiles calculated from PMFs at SAMs as well (Figure 7)—is reproduced very accurately. Because the curves in Figure 8 are calculated using only dielectric and repulsive ion–wall interactions, we conclude that the adsorption of Na^+ onto hydrophilic surfaces can be modeled as a purely dielectric effect. Furthermore, since the solvation repulsion $\mu_{\pm}^h(z)$ (eq 27) is unnecessary to model the ion density, we conclude that the water density depletion gap does not affect the distribution of small ions like Na^+ directly but only via the dielectric tensor.

Figure 9 shows the density of Cl^- ions at positively charged surfaces. Like the profiles for Na^+ at negatively charged surfaces, the Gouy–Chapman theory (model I in Table 2, black dashed lines) does not describe the simulation with explicit water (blue solid lines) correctly. At hydrophilic surfaces, the solution to the extended Poisson–Boltzmann equation (model III, blue dashed lines) performs much better for both surface charge densities (Figure 9a,c). In particular, the positions of the individual peaks is predicted correctly by the extended

Poisson–Boltzmann description (Figure 9b,d). At hydrophobic surfaces, on the other hand, the peak closest to the surface in the simulated Cl^- density does not appear in the extended Poisson–Boltzmann solution. Surprisingly, adding the hydration energy $\mu^h(z)$ (eq 27) to the non-electrostatic free energy hardly makes a difference (blue dashed lines in Figure 10). The

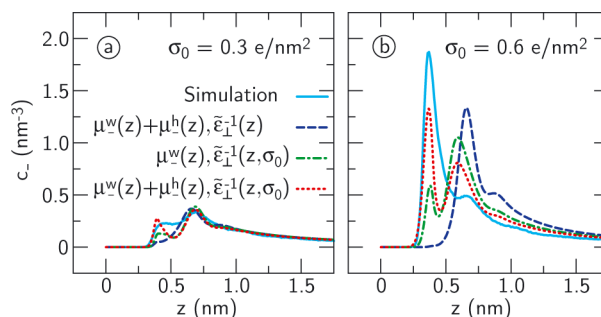


Figure 10. Density of chloride ions at hydrophobic diamond surfaces with a surface charge density of (a) $\sigma_0 = 0.3$ e nm⁻² and (b) $\sigma_0 = 0.6$ e nm⁻². Light blue solid lines denote the density profiles from simulations with explicit water. Other lines denote the density profiles using model III in Table 2, with different combinations of $\tilde{\epsilon}_{\perp}^{-1}(z)$ and $\mu_{-}(z)$. Blue dashed lines: wall and hydration energy, $\mu_{-}(z) = \mu_{-}^w(z) + \mu_{-}^h(z)$ (eqs 26 and 27), and $\tilde{\epsilon}_{\perp}^{-1}(z)$ at an uncharged surface (eqs 28 and 29 using $\lambda_d = 0.446$ nm). Green dash-dotted lines: only wall energy, $\mu_{-}(z) = \mu_{-}^w(z)$, and the dielectric profile $\tilde{\epsilon}_{\perp}^{-1}(z, \sigma_0)$ at nonzero external electric field. Red dotted lines: wall and hydration energy, $\mu_{-}(z) = \mu_{-}^w(z) + \mu_{-}^h(z)$, and $\tilde{\epsilon}_{\perp}^{-1}(z, \sigma_0)$. For $\tilde{\epsilon}_{\perp}^{-1}(z, \sigma_0)$, we use the dielectric profiles at external fields of (a) $D_{\perp}/\epsilon_0 = 4$ V/nm and (b) $D_{\perp}/\epsilon_0 = 8$ V/nm.²⁴

case of Cl^- at hydrophobic surfaces is special, however, not only because it has the biggest hydration energy of all cases shown in Figures 8 and 9 but also because the dielectric profile at positively charged hydrophobic surfaces differs from the profile at zero external electric field.²⁴ Therefore, we recalculate the Cl^- density profiles using the dielectric profile calculated in the presence of an external electric field and convoluted according to eqs 28 and 29, denoted $\tilde{\epsilon}_{\perp}^{-1}(z, \sigma_0)$, with and without hydration energy contribution (Figure 10). The same simulation profiles as those shown in Figure 9b and d are shown as blue solid lines. For $\sigma_0 = 0.3$ e nm⁻², which corresponds to $D_{\perp}(0)/\epsilon_0 = 5.4$ V/nm, we use $\epsilon_{\perp}^{-1}(z, \sigma_0)$ calculated at a homogeneous external field of $D_{\perp}/\epsilon_0 = 4$ V/nm, and for $\sigma_0 = 0.6$ e nm⁻² ($D_{\perp}(0)/\epsilon_0 = 10.8$ V/nm), we use the dielectric profile calculated at an external field strength of $D_{\perp}/\epsilon_0 = 8$ V/nm. At both values of the bare surface charge density σ_0 , a small peak appears at the correct position, already without hydration energy, $\mu_{-}(z) = \mu_{-}^w(z)$ (green dash-dotted lines). With hydration energy, $\mu_{-}(z) = \mu_{-}^w(z) + \mu_{-}^h(z)$, the peak increases significantly in size (red dotted lines). Although the height is still not captured correctly, the red dotted line reproduces the position of the Cl^- peak closest to the surface, which means that this peak is due to the combination of the hydration energy of big ions at hydrophobic surfaces and the dependence of the dielectric profile on the external electric field.

From the results shown in Figures 8–10, we conclude that the dielectric function, in conjunction with a mean-field electrostatic model (model III in Table 2), is sufficient to describe the main features of the distribution of simple (monovalent, monatomic) ions at charged aqueous interfaces at low ion concentration. Furthermore, the correspondence

between the simulated and calculated ion density profiles indicates that the distribution of small, non-polarizable ions at moderately charged hydrophilic and hydrophobic interfaces is largely determined by the dielectric profile of pure water and the repulsive ion–wall interaction $\mu_{\pm}^w(z)$. The hydration interaction $\mu_{\pm}^h(z)$ plays a role for larger ions at hydrophobic surfaces, but for Cl^- , the hydration energy is not the dominant factor (Figure 10). To reproduce the simulated density profiles of non-polarizable ions, it is necessary to convolute the dielectric profile with the size of the ion. Without convolution, the extended Poisson–Boltzmann equation yields qualitatively similar solutions, but the heights and positions of the peaks in the ion densities are different. We expect that polarizable ions, whose internal charge distribution is free to respond to the local dielectric environment, behave more like point charges, leading to sharper peaks and adsorption closer to the interface. Note that, whereas the solution to the Poisson–Boltzmann equation is largely insensitive to the non-electrostatic interaction energy strength B , the length scale λ_{LJ} does affect the results. The current model could be improved by an accurate determination of the full non-electrostatic energy profile.

■ ELEMENTARY MODEL OF INTERFACIAL CHARACTERISTICS

We will now calculate static and dynamic properties of aqueous interfaces using an even more simplified model (model IV in Table 2), aimed at capturing the physical properties of interfacial water layers at large distances from the interface. To this end, we approximate the dielectric profile and the viscosity by step functions. Clearly, the small-scale ion-specific effects shown in Figures 8–10 will not be preserved. The dielectric variation at the interface is accounted for by using a step function at the position of the dielectric dividing surface

$$\epsilon_{\perp}^{-1}(z) = \begin{cases} 1 & \text{if } z < z_{\perp}^{\text{DDS}} \\ \epsilon_{\text{bulk}}^{-1} & \text{otherwise} \end{cases} \quad (31)$$

with z_{\perp}^{DDS} defined in eq 16b. The profile of eq 31 is designed to preserve the voltage difference between the surface and the bulk fluid obtained using the full dielectric profile $\epsilon_{\perp}^{-1}(z)$. To simplify the hydrodynamic model, we also approximate the variations in interfacial viscosity by a step function, located at the plane of shear z_s

$$\eta(z) = \begin{cases} \eta_i & \text{if } z < z_s \\ \eta_{\text{bulk}} & \text{otherwise} \end{cases} \quad (32)$$

with η_i being the viscosity in the interfacial layer of width z_s and η_{bulk} being the bulk viscosity. At the hydrophobic surface, z_s is taken to be the width of the depletion layer ($z_s = 0.15$ nm), and the parameters for the hydrophilic surface are taken from ref 27. Far from the interface, the step function profile of eq 32 gives rise to the same flow profile as the one obtained from the boundary condition of eq 18, with an apparent slip length given by

$$b = z_s(\eta_{\text{bulk}}/\eta_i - 1) \quad (33)$$

The electrophoretic mobility of the ions $\nu_{\pm}(z)$, which is important for the conductivity of the fluid, depends on the ion concentration, fluid viscosity, and proximity to the surface. In the elementary model, we only take bulk-like drag into account, leading to

$$\nu_{\pm}(z) = \nu_{\pm} \begin{cases} \eta_{\text{bulk}}/\eta_i & \text{if } z < z_s \\ 1 & \text{otherwise} \end{cases} \quad (34)$$

with ν_{\pm} being the bulk electrophoretic mobility. We will scrutinize the effect of a more realistic electrophoretic mobility profile further below. It is important to note that model IV only preserves the electrostatic properties far away from the interface, and not the local profile. In fact, the main effect of the dielectric profile is condensed into a layer of width z_{\perp}^{DDS} . Because the spatial correlation between the electrostatic and non-electrostatic contributions to the free energy is important for the ion distribution, the non-electrostatic potential of eqs 26 and 27 cannot be used in conjunction with the simplified model. Instead, we use an exponential function as an effective description of the non-electrostatic contribution to the potential, based on a single length scale

$$\mu_{\pm}^e(z) = \alpha \exp[1 - 2z/\lambda_{\pm}] \quad (35)$$

with α being a fit parameter. We use $\lambda_{\pm} = 0.3$ nm as the diameter of a typical ion. Equation 35 provides a heuristic description of the effective repulsion or attraction of ions due to non-electrostatic effects.

■ DOUBLE-LAYER CAPACITANCE

The surface charge on a charged interface and the associated counterions form a capacitor, whose capacitance is determined by the distance between the ions and the surface, as well as the dielectric properties of the medium. As stated in the Introduction, the Gouy–Chapman theory (black dashed lines in Figure 11) overestimates measured values of the double-layer

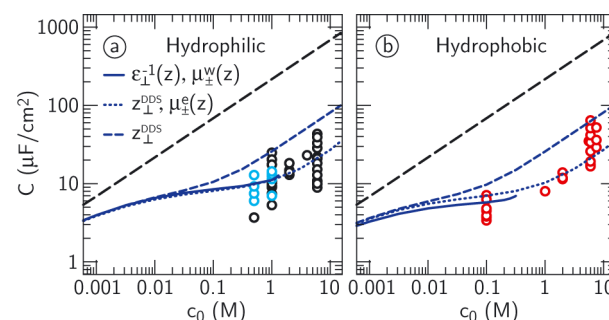


Figure 11. Double-layer capacitance C as a function of the bulk salt concentration c_0 . Colored symbols represent experimental results on different kinds of (a) hydrophilic and (b) hydrophobic carbon-based surfaces.²³ The black symbols in part a represent data at surfaces with unknown contact angle. Lines represent solutions to the extended Poisson–Boltzmann equation using the different models from Table 2. Black dashed lines: $\epsilon_{\perp}^{-1}(z) = \epsilon_{\text{bulk}}^{-1}$ with $\mu_{\pm}(z) = 0$ (model I, Gouy–Chapman). Blue solid lines: $\epsilon_{\perp}^{-1}(z)$ from Figure 3 (no convolution) and $\mu_{\pm}(z) = \mu_{\pm}^w(z)$ for NaCl (model III). Blue dashed lines: $\epsilon_{\perp}^{-1}(z)$ from eq 31 with $\mu_{\pm}(z) = 0$ (model IV). Blue dotted lines: $\epsilon_{\perp}^{-1}(z)$ from eq 31 with $\mu_{\pm}(z) = \mu_{\pm}^e(z)$ from eq 35 using $\alpha = 1$ (model IV). For z_{\perp}^{DDS} , we use the values from Table 1.

capacitance (symbols in Figure 11) by an order of magnitude. Although this discrepancy is accounted for by the Stern layer model, which postulates an interfacial layer of low dielectric constant, the Stern model only yields the ratio δ/ϵ_i of the width δ and the dielectric constant ϵ_i of this layer.¹⁹ The dielectric profile shown in Figure 3 gives a more detailed description of the dielectric properties of the interfacial layer, and the double-layer capacitance can be calculated directly from the extended

Poisson–Boltzmann equation (eqs 21–25). The first test of the simplified model of the dielectric interface presented here is whether it reproduces the experimental double-layer capacitance.

We calculate the differential double-layer capacitance $C = d\sigma_0/d\psi_0$ from eqs 21–25, with ψ_0 being the electrostatic potential at $z = 0$. The equation is solved in the limit of low surface charge density, $\sigma_0 \rightarrow 0$, where eq 21 can be linearized (Debye–Hückel approximation) and the steric interaction contained in eq 24 vanishes. First, we use the dielectric profile $\varepsilon_{\perp}^{-1}(z)$ shown in Figure 3 and the non-electrostatic interaction $\mu_{\pm}(z) = \mu_{\pm}^w(z)$ from eq 26 (model III in Table 2), of which we know to reproduce the simulated ion density profiles. The calculated capacitance curves (solid lines in Figure 11) lie an order of magnitude below the Gouy–Chapman curves, fitting the experimental data at low salt concentration well. At higher salt concentration, the Poisson–Boltzmann equation cannot be integrated using the full dielectric profile, presumably because the Debye length approaches the typical length scale of the variation in the dielectric profile ($z_{\perp}^{\text{DBS}} \sim 0.1$ nm), where the local approximation of eq 20 breaks down. Using the approximation of eq 31 (model IV in Table 2 with parameters from Table 1) without non-electrostatic interaction ($\mu_{\pm}(z) = 0$; blue dashed lines in Figure 11), the calculated capacitance curves lead through the upper limit of the experimental data. Incorporating the heuristic non-electrostatic interaction of eq 35, the experimental values can be reproduced quite accurately, using α as a fit parameter. The dotted lines in Figure 11 show the curves for $\alpha = 1$ and $\lambda_{\pm} = 0.3$ nm, which produces similar curves as the ones obtained from the full $\varepsilon_{\perp}^{-1}(z)$ with the surface repulsion $\mu_{\pm}^w(z)$.

ELECTROKINETIC FLOW

The successful replication of the simulated ion density profiles and the double-layer capacitance experiments suggests that the extended Poisson–Boltzmann model captures the static ion distribution correctly. Moreover, the double-layer capacitance can be modeled successfully by the step function approximation of eq 31, using $\mu_{\pm}(z) = \mu_{\pm}^w(z)$ from eq 35 to fit the experimental data. In conjunction with the viscosity profile calculated in the previous sections, we now formulate a dynamic description to model electrokinetic experiments, based on the same step function approximations. The basic setup of the electrokinetic measurements that we consider consists of a charged planar surface in contact with an aqueous electrolyte of monovalent ions. In response to a parallel applied electric field E_{\parallel} , counterions move along the surface, leading to an electro-osmotic flow profile $u_{\parallel}(z)$. At the same time, the excess concentration of counterions at the interface produces an electric conductivity exceeding the bulk value. We calculate the electro-osmotic mobility and the conductivity in terms of their equivalent surface charge densities and compare the results to experimental data.

For laminar flows, $u_{\parallel}(z)$ is calculated from the Stokes equation

$$\nabla\eta(z)\nabla u_{\parallel}(z) = -P_0(z)E_{\parallel} \quad (36)$$

with spatially varying viscosity $\eta(z)$ and ionic charge density $P_0(z)$. Note that static homogeneous electric fields do not couple to higher order electric moments, as shown earlier,^{66,67} which is why higher-order multipole moments do not appear in

eq 36. The electro-osmotic mobility is found by integrating eq 36 twice using $u_{\parallel}(z) = 0$ as a boundary condition

$$\frac{u_{\parallel}(z)}{E_{\parallel}} = -\int_0^z \frac{D_{\perp}(z')}{\eta(z')} dz' \quad (37)$$

with $D_{\perp}(z)$ being the displacement field perpendicular to the surface, which obeys $\nabla D_{\perp}(z) = P_0(z)$. The scale of experimental setups implies that the electro-osmotic velocity $u_{\parallel}(z)$ is measured far away from the interface, in the limit $z \rightarrow \infty$. In the Gouy–Chapman model, $\varepsilon_{\perp}^{-1}(z) = \varepsilon_{\text{bulk}}^{-1}$, and assuming $\eta(z) = \eta_{\text{bulk}}$ in eq 37, the measured electro-osmotic mobility is given by the Helmholtz–Smoluchowski equation

$$\lim_{z \rightarrow \infty} \frac{u_{\parallel}(z)}{E_{\parallel}} = -\frac{\varepsilon_0 \varepsilon_{\text{bulk}}}{\eta_{\text{bulk}}} \zeta \quad (38)$$

with the electrostatic potential at $z = 0$ being given by

$$\zeta = \int_0^{\infty} \frac{D_{\perp}(z)}{\varepsilon_0 \varepsilon_{\text{bulk}}} dz \quad (39)$$

which is known as the zeta potential. Because the surface potential is typically not measured directly, it is often more convenient to express ζ in terms of the equivalent surface charge density. Combining the standard Poisson–Boltzmann relation with the charge neutrality boundary condition leads to the Graham equation, relating ζ to the electrokinetic surface charge density σ_{ek}

$$\sigma_{\text{ek}} = \sqrt{\frac{8c_0\varepsilon_0\varepsilon_{\text{bulk}}}{\beta}} \sinh\left[\frac{\beta e\zeta}{2}\right] \quad (40)$$

with c_0 being the bulk salt concentration. The zeta potential is calculated using eq 38, where the electro-osmotic mobility far from the interface is either measured experimentally or calculated from eq 37.

In addition to the electrokinetic mobility, the excess ionic charge density at a charged surface gives rise to an enhanced electric conductivity with respect to the bulk fluid.^{68–70} This surface conductivity can be conveniently measured in nano-fluidic channels at low salt concentration, in which case the contribution from the bulk electrolyte vanishes.⁷¹ The conductivity of the electrolyte comprises a convective part, due to the electro-osmotic flow $u_{\parallel}(z)$, and an intrinsically conductive part, due to the electrophoretic mobility of the ions $\nu_{\pm}(z)$. We define the surface conductivity by subtracting the bulk contribution $e(\nu_+ + \nu_-)c_0$ from the total conductivity, leading to

$$\begin{aligned} \frac{I}{E_{\parallel}} &= \int_0^{\infty} e[c_+(z) - c_-(z)][u_{\parallel}(z)/E_{\parallel}] dz \\ &+ \int_0^{\infty} e[\nu_+(z)c_+(z) + \nu_-(z)c_-(z) - (\nu_+ + \nu_-)c_0] dz \end{aligned} \quad (41)$$

with ν_{\pm} being the bulk electrophoretic mobility of the positive and negative ions. In the Gouy–Chapman model, we ignore the z dependence of the electrophoretic mobility. Since the salt types considered in the experiments that we compare our results with are KCl and KNO₃, we assume $\nu_+ = \nu_- = \nu$, which is a good approximation for both KCl and KNO₃. For the numerical calculations, we take $\nu = 8 \times 10^{10}$ nm²/(V s). With these assumptions, the surface conductivity can be expressed as

an equivalent surface charge density similar to the Graham equation (eq 40)

$$\sigma_c = \frac{\kappa^2 \eta_{\text{bulk}}}{4\epsilon c_0 + \nu \kappa^2 \eta_{\text{bulk}}} \sqrt{\frac{I}{E_{\parallel}}} \sqrt{\frac{I}{E_{\parallel}} + \frac{32e^2 c_0^2}{\kappa^3 \eta_{\text{bulk}}} + \frac{8\epsilon c_0 \nu}{\kappa}} \quad (42)$$

with κ being the inverse Debye screening length, defined as $\kappa = (2e^2 c_0 / \epsilon_0 \epsilon_{\text{bulk}})^{1/2}$. For derivations of eqs 40 and 42, we refer to ref 72.

With σ_0 , σ_{ek} , and σ_c , we have three measures of the surface charge density, which—by definition—are equivalent within the Gouy–Chapman model. However, experiments give very different results. First of all, the electrokinetic surface charge density σ_{ek} saturates as a function of the bare surface charge density σ_0 .^{73–75} Interestingly, this saturation occurs at both hydrophilic and hydrophobic surfaces. Experimental data of σ_{ek} for KNO₃ at hydrophilic TiO₂ and FeOOH, and at hydrophobic AgI surfaces are shown as symbols in Figure 12,

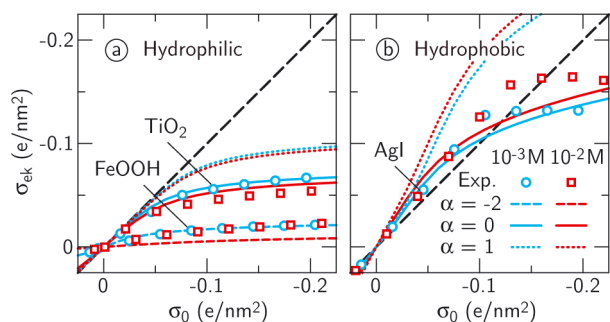


Figure 12. Electrokinetic surface charge density σ_{ek} as a function of the bare surface charge density σ_0 at (a) two different hydrophilic substrates (TiO₂ and FeOOH) and (b) a hydrophobic substrate (AgI). Symbols denote a discretization of the experimental data presented in ref 73 for KNO₃ at $c_0 = 10^{-2}$ M and $c_0 = 10^{-3}$ M. In order to cancel the surface conduction correction,⁷³ the hydrophilic curves have been reconstructed according to $\sigma_{\text{ek}} = \sinh(\sinh^{-1}(\sigma_{\text{ek}}^{\text{corr}})/1.55)$, with $\sigma_{\text{ek}}^{\text{corr}}$ corresponding to the values reported in ref 73. Curves denote solutions to eqs 21–25 using model IV in Table 2 (dielectric profile from eq 31, non-electrostatic interactions from eq 35, and viscosity from eq 32). For the hydrophilic curves, $z_{\text{L}}^{\text{DDS}} = 0.10$ nm, $z_s = 0.4$ nm, and $\eta_i = 4\eta_{\text{bulk}}$ giving $b = -0.3$ nm. For the hydrophobic curves, $z_{\text{L}}^{\text{DDS}} = 0.12$ nm, $z_s = 0.15$ nm, and $\eta_i = \eta_{\text{bulk}}/15$, giving $b = 2.1$ nm. Results are shown for different values of the fit parameter α in eq 35.

together with the Gouy–Chapman model (black dashed lines). In a classical explanation, enhanced interfacial viscosity is responsible for the saturation.^{73,74} As we have shown in Figure 5, however, the interfacial viscosity is only enhanced at hydrophilic surfaces; at hydrophobic surfaces, we would expect an increased electrokinetic surface charge density due to the fluid slipping along the surface. The second important experimental result is that the conductive surface charge density σ_c , which can be measured simultaneously with σ_{ek} in nanochannels, exceeds σ_{ek} .^{50,71,76–80} In other words, whereas the electro-osmotic flow saturates as a function of the bare surface charge density, the electric current does not, a phenomenon that is referred to as *anomalous surface conduction*.⁸¹ In Figure 13, we show experimental results of σ_c versus σ_{ek} for KCl in hydrophilic silica channels and at silica particles, and for KCl at hydrophobic polystyrene particles. Classically, the discrepancy between electrokinetic and conductive surface charge density is explained by the

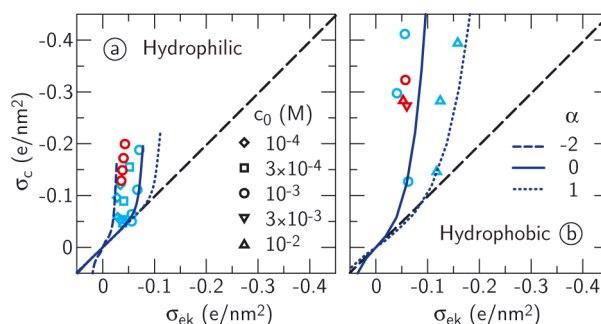


Figure 13. Conductive surface charge density σ_c as a function of the electrokinetic surface charge density σ_{ek} for different substrates in contact with a KCl solution of bulk concentration c_0 . (a) Data from rectangular silica channels (blue symbols⁵⁰) and monodisperse porous silica particles (red symbols⁸⁶). (b) Data from monodisperse spherical polystyrene particles (blue⁷⁷ and red symbols⁸⁷). Curves denote solutions to eqs 21–25 using model IV in Table 2 (dielectric profile from eq 31, non-electrostatic interactions from eq 35, viscosity from eq 32, and electrophoretic mobility from eq 34). We use the same interaction strengths as in Figure 12, $\alpha = -2$, $\alpha = 0$, and $\alpha = 1$, and a bulk concentration of 1 mM.

disconcerting assumption that the interfacial water layer, despite being stagnant for hydrodynamic transport, provides an alternative route for conductive transport.^{70,75,79,80,82–85}

To explain the experimental data discussed above, we solve the extended Poisson–Boltzmann equation with the approximate dielectric profile of eq 31 (model IV in Table 2 with parameters listed in Table 1) as a function of the bare surface charge density σ_0 at hydrophilic and hydrophobic diamond surfaces. Using the viscosity profile from eq 32 (shown as dashed lines in Figure 5), we calculate σ_{ek} and σ_c from eqs 40 and 42. The parameters for the viscosity profiles are $z_s = 0.4$ nm and $\eta_i = 4\eta_{\text{bulk}}$ at hydrophilic surfaces, producing an apparent slip length of $b = -0.3$ nm (eq 33), and $z_s = 0.15$ nm and $\eta_i = \eta_{\text{bulk}}/15$ at hydrophobic surfaces, producing $b = 2.1$ nm.²⁷ Without non-electrostatic interaction, our model results for σ_{ek} saturate as a function of σ_0 at both surface types (solid lines in Figure 12), in accordance with experimental results. Relative to the Gouy–Chapman model, the dielectric profile causes a lower electrokinetic mobility at both surface types, because the ions accumulate closer to the interface. At the hydrophilic surface, the enhanced viscosity works in the same direction, and indeed, a higher salt concentration decreases the average distance between the ions and the surface and therefore increases the influence of the high viscosity. At the hydrophobic surface, we see the same effect from the dielectric profile: ions accumulate closer to the interface, limiting the mobility. The viscosity profile, however, works in the opposite direction. For small σ_0 , the viscosity effect prevails, causing σ_{ek} to exceed σ_0 , whereas, for large σ_0 , the dielectric profile prevails, causing the saturation. This qualitatively correct behavior shows that the effect of the dielectric profile on the charge distribution is sufficient to explain the saturation of the electrokinetic surface charge density at both surface types. Nevertheless, using the non-electrostatic interaction from eq 35 with $\alpha = 1$, which fits the double-layer capacitance shown in Figure 11, the agreement with experimental data becomes worse (dotted lines in Figure 12). Whereas the data for TiO₂ and AgI can be fitted reasonably well with $\alpha = 0$, an attractive non-electrostatic contribution is necessary to fit the experimental data at FeOOH; in Figure 12, we show results for $\alpha = -2$. Moreover,

when looking at the static ion density profiles from the Poisson–Boltzmann model with the full dielectric profile and a repulsive non-electrostatic interaction, the contrast becomes more pronounced. The non-electrostatic interaction needed to reproduce the simulated profiles at the hydrophobic surface (Figures 8 and 9) is strong enough to partly compensate for the attractive effect of the dielectric profile, partly canceling the saturation effect. As a possible explanation for the discrepancy between the static double-layer capacitance and the electrokinetic results, we evaluate in the next section the influence that the shape of the space dependence of the ion mobility $\nu_{\pm}(z)$ might have. Another explanation for the discrepancy can possibly be found in our neglect of electrofriction effects, which arise in systems with inhomogeneously charged surfaces.^{88–90} Electrofriction can, for example, be calculated from the z dependent amplitude of the electrostatic potential oscillations due to a square array of discrete point charges on the surface.⁹¹ An effective friction coefficient can be derived from the solution to the Fokker–Planck equation describing the motion of an ion in that corrugated potential.⁹² Finally, a charge-induced increase of the local viscosity,⁶⁰ in combination with the finite ion size,⁹³ can possibly affect the fluid flow as well.

In Figure 13, we show the conductive surface charge density σ_c (eq 42) as a function of σ_{ek} for the same model parameters as used for Figure 12. Although the experimental results are taken at several different salt concentrations, we only show the model results for $c_0 = 1$ mM, because c_0 has little influence on the curves at low salt concentration. With the same range of non-electrostatic interaction strengths as used to fit the electrokinetic surface charge density (Figure 12), the model captures the experimental data at both surface types. The curves in Figure 13 rise because, while limiting σ_{ek} , the dielectric profile hardly affects the conductivity, explaining the anomalous surface conduction. The fit curves in Figure 13a and b have been calculated for the same range of the bare surface charge density, $\sigma_0 > -0.75$ e nm⁻². In accordance with the experimental results, the calculated σ_c values remain lower at hydrophilic surfaces (Figure 13a) than at hydrophobic surfaces (Figure 13b), as can be seen from the curves ceasing around $\sigma_c \approx -0.2$ e nm⁻² in Figure 13a.

IONIC ELECTROPHORETIC MOBILITY PROFILE

The shape of the ionic mobility profile $\nu_{\pm}(z)$, which has not been examined in the previous section, has an influence on the conductive surface charge density σ_c , cf. eqs 41 and 42. To estimate the extent of the effect of $\nu_{\pm}(z)$, we use the ionic mobility of a sphere of diameter λ_{\pm} at a distance $z > \lambda_{\pm}/2$ from a planar wall with a no-slip boundary condition, calculated from the hydrodynamic interactions on the Rotne–Prager level,^{90,94}

$$\nu_{\pm}(z) = \nu_{\pm} \left(1 - \frac{9\lambda_{\pm}}{32z} + \frac{1}{64} \left(\frac{\lambda_{\pm}}{z} \right)^3 \right) + O(\lambda_{\pm}^4) \quad (43)$$

with ν_{\pm} being the bulk electrophoretic mobility. We set $\nu_{\pm}(z) = 0$ for $z < \lambda_{\pm}/2$. The electrophoretic mobility profiles are shown in Figure 14d for different values of the ion diameter λ_{\pm} . Because the spatial correlation between the mobility profile and the ion density is important, we cannot use the step function approximation of eq 31 (model IV in Table 2), as it only preserves the electrostatic potential far from the interface and not the local profile. Therefore, we solve the extended Poisson–Boltzmann equation using model III in Table 2. For the dielectric profile, we take $\tilde{\epsilon}_{\perp}^{-1}(z)$ at a hydrophilic interface,

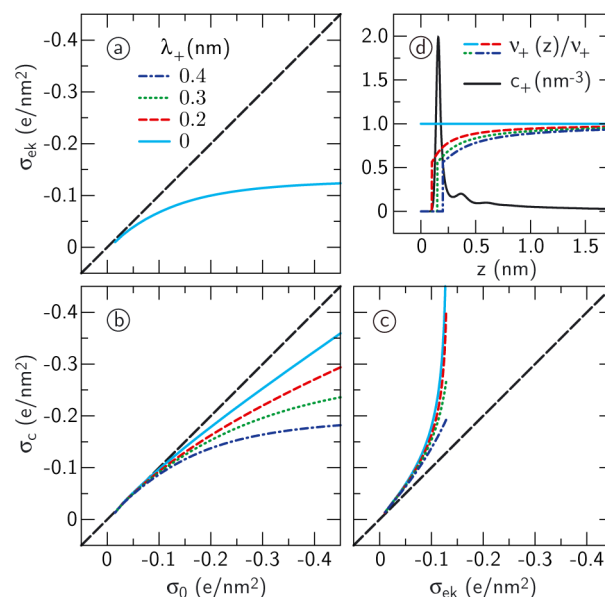


Figure 14. (a) Electrokinetic surface charge density (eq 40) as a function of bare surface charge density and conductive surface charge density (eq 42) as a function of (b) bare and (c) electrokinetic surface charge density, using model III in Table 2. For the ionic mobility profiles $\nu_{\pm}(z)$, we use eq 43 with different ionic diameters λ_{\pm} , shown as colored lines in part d. Shown as a black solid line in part d is the counterion density calculated from the extended Poisson–Boltzmann equation at a bare surface charge density of $\sigma_0 = -0.3$ e nm⁻². The bulk salt concentration is $c_0 = 1$ mM, and the dielectric profile is $\tilde{\epsilon}_{\perp}^{-1}(z)$ for Na⁺ at a hydrophilic surface.

using the Na⁺ dielectric diameter $\lambda_d = 0.330$ nm for the convolution of eq 28. For the viscosity $\eta(z)$, we use the profile from MD simulations shown as a solid line in Figure 5a, and $\eta_{\text{bulk}} = 1 \times 10^{-30}$ Js/nm⁻³. We solve the equation at a bare surface charge density of -0.75 e nm⁻² $< \sigma_0 < 0$ e nm⁻², using a bulk salt concentration density of $c_0 = 1$ mM, so the co-ion density is irrelevant. We take $\nu_{\pm} = 8 \times 10^{10}$ nm²/(V s) for the bulk ion mobility, as we did earlier.

As shown in Figure 14a, the electrokinetic surface charge density σ_{ek} shows the same saturation with increasing bare surface charge density as shown previously for the step-function profiles of model IV (Figure 12), and is independent of the mobility profile. The conductive surface charge density σ_c depends markedly on the ion diameter λ_{\pm} used in the mobility profile, decreasing as λ_{\pm} increases (Figure 14b). However, plotting σ_c as a function of σ_{ek} (Figure 14c) produces very similar curves to the ones produced by model IV (Figure 13), showing that the z dependence of the ionic mobility is obscured when considering the relation between the conductivity and the electrophoretic mobility.

CONCLUSIONS

The aim of the work described in this paper is to incorporate information about the molecular structure of interfacial water into the description of the static and dynamic properties of charged solutes in electrolyte solution, using molecular simulation techniques to complement continuum theory. The use of continuum theory enables us to reach time and length scales that are unattainable using only molecular simulations. At the same time, it provides us with the flexibility to easily vary system parameters such as salt concentration and surface charge density.

Incorporating the dielectric profile of water into the Poisson–Boltzmann equation, we first study the static ion distributions at hydrophilic and hydrophobic interfaces. We show in Figures 8 and 9 that the pronounced peaks and dips in the distribution of non-polarizable ions found in atomistic MD simulations can be ascribed to the effect of the dielectric profile and a simple non-electrostatic repulsion from the wall. Overall, the dielectric profile gives rise to ion adsorption due to the steep increase of the potential at charged interfaces. However, the non-electrostatic repulsion from the interface partly compensates for the dielectric attraction. Therefore, the dielectric adsorption peak is most pronounced for small ions, such as Na^+ , which explains the adsorption peak seen in the potential of mean force at hydrophilic SAMs. Importantly, the dielectric profiles have to be convoluted with the size of the dielectric cavity in which the ion resides, which we expect to depend on ion polarizability. The image charge repulsion, which is expected to play a role in the PMF of single ions at interfaces, is not necessary to model ion distributions at charged interfaces, even at very low concentrations. To model the adsorption of Cl^- at hydrophobic surfaces, it is necessary to use nonlinear dielectric response theory. Hydration energy provides a significant additional attractive potential for relatively big ions—the size of Cl^- and larger—but the effect is not decisive for adsorption of Cl^- at hydrophobic surfaces.

One of the most significant advantages of the combination of molecular detail from the MD simulations with the large scale of continuum theory is that it allows for direct comparison with experimental data. Our two-scale modeling approach thus provides us with the means for experimental verification of our theoretical models, and simultaneously offers new insight into the molecular origin of experimental observations. Comparison of the double-layer capacitance calculated from our two-scale model with capacitance measurements at hydrophilic and hydrophobic carbon-based surfaces shows that incorporating the dielectric profile of pure water yields a double-layer capacitance of the right order of magnitude. Good agreement with experimental data is obtained using an additional repulsive non-electrostatic potential.

To study the dynamic properties of charged aqueous solutes, we combine the extended Poisson–Boltzmann model with the Stokes equation, where the viscosity profile is obtained from MD simulations. This electrokinetic model qualitatively captures the experimentally observed saturation of the electro-osmotic mobility at charged surfaces as a function of bare surface charge, as well as the so-called *anomalous surface conductivity*. The physical mechanism responsible for both effects is the adsorption of ions in the dielectric environment of the surface. However, the additional non-electrostatic potential needed to reproduce the experimental electrophoretic data quantitatively does not match the repulsive non-electrostatic potential needed to reproduce the double-layer capacitance and the static ion density profiles. This discrepancy could be due to surface roughness or electrofriction effects.^{89,90}

Further research is needed to understand viscous effects at charged interfaces and their relation to surface type, corrugation, and charge distribution. Furthermore, the effect of finite ion concentrations on the dielectric profile, and the influence of the ion model, in particular the ion polarizability and Lennard-Jones interaction parameters, on the response of the ion to its dielectric environment deserves attention. Finally, the limits of applicability of the simplified model and rigorous methods for the extraction of the non-electrostatic interaction

potential from molecular data remain to be studied in more detail.

AUTHOR INFORMATION

Corresponding Author

*E-mail: douwe.bonthuis@physics.ox.ac.uk. Phone: +44-1865-273995.

Notes

The authors declare no competing financial interest.

Biographies



Douwe Jan Bonthuis studied applied physics at Delft University of Technology and Harvard University. He did his Ph.D. in theoretical soft matter physics with Roland R. Netz at the Technical University of Munich, focusing on the molecular properties of aqueous interfaces. Since 2012, he holds a position as a Glasstone Fellow at the Rudolf Peierls Centre for Theoretical Physics, University of Oxford.



Roland R. Netz studied physics at the Technical University of Berlin and at MIT and received his Ph.D. in 1994 from the University of Cologne. After postdocs at Tel-Aviv University, UCSB, Seattle, Institute Charles Sadron in Strasbourg, and CEA in Paris, he was a research associate at the Max-Planck Institute for Colloids and Interfaces in Potsdam. He was appointed associate professor of physics at the LMU Munich in 2002 and full professor of physics at the TU Munich in 2004. Since 2011, he has held a chair in theoretical bio-soft matter physics at the Free University of Berlin.

ACKNOWLEDGMENTS

We acknowledge financial support from the German-Israeli Foundation for Scientific Research and Development (GIF) in the project “Ion specific interactions between functionalized surfaces”, the Deutsche Forschungsgemeinschaft (DFG) in the collaborative research center SFB 1078, as well as funding from

a Glasstone Research Fellowship and Linacre College, Oxford University.

REFERENCES

- (1) Ball, P. Water as an Active Constituent in Cell Biology. *Chem. Rev.* **2008**, *108*, 74–108.
- (2) Stone, H. A.; Stroock, A. D.; Ajdari, A. Engineering Flows in Small Devices: Microfluidics toward a Lab-On-A-Chip. *Annu. Rev. Fluid Mech.* **2004**, *36*, 381–411.
- (3) Squires, T. M.; Quake, S. R. Microfluidics: Fluid Physics at the Nanoliter Scale. *Rev. Mod. Phys.* **2005**, *77*, 977–1026.
- (4) Schoch, R. B.; Han, J.; Renaud, P. Transport Phenomena in Nanofluidics. *Rev. Mod. Phys.* **2008**, *80*, 839–883.
- (5) Lang, E. W.; Lüdemann, H.-D. Anomalies of Liquid Water. *Angew. Chem., Int. Ed.* **1982**, *21*, 315–329.
- (6) a Bopp, P.; Kornyshev, A. A.; Sutmann, G. Static Nonlocal Dielectric Function of Liquid Water. *Phys. Rev. Lett.* **1996**, *76*, 1280.
- (7) Du, X.; Guo, P.; Song, H.; Chen, X. Vibrational Spectroscopy of Water at the Vapor Water Interface. *Phys. Rev. Lett.* **1993**, *70*, 2313.
- (8) Du, Q.; Freysz, E.; Shen, Y. R. Vibrational-Spectra of Water-Molecules at Quartz Water Interfaces. *Phys. Rev. Lett.* **1994**, *72*, 238.
- (9) Verwey, E. J. W. The Electrical Double Layer and the Stability of Lyophobic Colloids. *Chem. Rev.* **1935**, *16*, 363–415.
- (10) Hidalgo-Álvarez, R.; Martín, A.; Fernández, A.; Bastos, D.; Martínez, F.; De Las Nieves, F. Electrokinetic Properties, Colloidal Stability and Aggregation Kinetics of Polymer Colloids. *Adv. Colloid Interface Sci.* **1996**, *67*, 1–118.
- (11) Marčelja, S.; Radić, N. Repulsion of Interfaces due to Boundary Water. *Chem. Phys. Lett.* **1976**, *42*, 129–130.
- (12) Schneck, E.; Sedlmeier, F.; Netz, R. R. Hydration Repulsion between Biomembranes Results from an Interplay of Dehydration and Depolarization. *Proc. Natl. Acad. Sci. U.S.A.* **2012**, *109*, 14405–14409.
- (13) Chandler, D. Interfaces and the Driving Force of Hydrophobic Assembly. *Nature* **2005**, *437*, 640–647.
- (14) Levy, Y.; Onuchic, J. N. Water Mediation in Protein Folding and Molecular Recognition. *Annu. Rev. Biophys. Biomol. Struct.* **2006**, *35*, 389–415.
- (15) Snyder, P. W.; Mecnović, J.; Moustakas, D. T.; Thomas, S. W.; Harder, M.; Mack, E. T.; Lockett, M. R.; Héroux, A.; Sherman, W.; Whitesides, G. M. Mechanism of the Hydrophobic Effect in the Biomolecular Recognition of Arylsulfonamides by Carbonic Anhydrase. *Proc. Natl. Acad. Sci. U.S.A.* **2011**, *108*, 17889–17894.
- (16) Li, I. T. S.; Walker, G. C. Signature of Hydrophobic Hydration in a Single Polymer. *Proc. Natl. Acad. Sci. U.S.A.* **2011**, *108*, 16527–16532.
- (17) Schwendel, D.; Hayashi, T.; Dahint, R.; Pertsin, A.; Grunze, M.; Steitz, R.; Schreiber, F. Interaction of Water with Self-Assembled Monolayers: Neutron Reflectivity Measurements of the Water Density in the Interface Region. *Langmuir* **2003**, *19*, 2284–2293.
- (18) López-León, T.; Santander-Ortega, M. J.; Ortega-Vinuesa, J. L.; Bastos-González, D. Hofmeister Effects in Colloidal Systems: Influence of the Surface Nature. *J. Phys. Chem. C* **2008**, *112*, 16060–16069.
- (19) Stern, O. Zur Theorie der Elektrolytischen Doppelschicht. *Z. Elektrochem.* **1924**, *30*, 508–516.
- (20) Blum, L.; Henderson, D. Mixtures of Hard Ions and Dipoles against a Charged Wall - The Ornstein-Zernike Equation, Some Exact Results, and the Mean Spherical Approximation. *J. Chem. Phys.* **1981**, *74*, 1902–1910.
- (21) Kharkats, Y. I.; Kornyshev, A. A.; Vorotyntsev, M. A. Electrostatic Models in Theory of Solutions. *J. Chem. Soc., Faraday Trans. 2* **1976**, *72*, 361–371.
- (22) Kornyshev, A. A.; Schmickler, W.; Vorotyntsev, M. A. Nonlocal Electrostatic Approach to the Problem of a Double Layer at a Metal-Electrolyte Interface. *Phys. Rev. B* **1982**, *25*, 5244–5256.
- (23) Bonthuis, D. J.; Gekle, S.; Netz, R. R. Dielectric Profile of Interfacial Water and Its Effect on Double-Layer Capacitance. *Phys. Rev. Lett.* **2011**, *107*, 166102.
- (24) Bonthuis, D. J.; Gekle, S.; Netz, R. R. Profile of the Static Permittivity Tensor of Water at Interfaces: Consequences for Capacitance, Hydration Interaction and Ion Adsorption. *Langmuir* **2012**, *28*, 7679–7694.
- (25) Honig, C. D. F.; Ducker, W. A. No-Slip Hydrodynamic Boundary Condition for Hydrophilic Particles. *Phys. Rev. Lett.* **2007**, *98*, 028305.
- (26) Joly, L.; Ybert, C.; Trizac, E.; Bocquet, L. Liquid Friction on Charged Surfaces: From Hydrodynamic Slippage to Electrokinetics. *J. Chem. Phys.* **2006**, *125*, 204716.
- (27) Sendner, C.; Horinek, D.; Bocquet, L.; Netz, R. R. Interfacial Water at Hydrophobic and Hydrophilic Surfaces: Slip, Viscosity, and Diffusion. *Langmuir* **2009**, *25*, 10768–10781.
- (28) Lauga, E.; Brenner, M. P.; Stone, H. A. *Microfluidics: the No-Slip Boundary Condition*; Springer: New York, 2007; Chapter 19, p 1219.
- (29) Kunz, W. Specific Ion Effects in Colloidal and Biological Systems. *Curr. Opin. Colloid Interface Sci.* **2010**, *15*, 34–39.
- (30) Horinek, D.; Serr, A.; Bonthuis, D. J.; Boström, M.; Kunz, W.; Netz, R. R. Molecular Hydrophobic Attraction and Ion-Specific Effects Studied by Molecular Dynamics. *Langmuir* **2008**, *24*, 1271–1283.
- (31) Schwier, N.; Horinek, D.; Netz, R. R. Reversed Anionic Hofmeister Series: the Interplay of Surface Charge and Surface Polarity. *Langmuir* **2010**, *26*, 7370–7379.
- (32) Schwier, N.; Horinek, D.; Netz, R. R. Anionic and Cationic Hofmeister Effects on Hydrophobic and Hydrophilic Surfaces. *Langmuir* **2013**, *29*, 2602–2614.
- (33) Omta, A. W.; Kropman, M. F.; Woutersen, S.; Bakker, H. J. Negligible Effect of Ions on the Hydrogen-Bond Structure in Liquid Water. *Science* **2003**, *301*, 347–349.
- (34) Berendsen, H. J. C.; Grigera, J. R.; Straatsma, T. P. The Missing Term in Effective Pair Potentials. *J. Phys. Chem.* **1987**, *91*, 6269–6271.
- (35) Van der Spoel, D.; Lindahl, E.; Hess, B.; Groenhof, G.; Mark, A. E.; Berendsen, H. J. GROMACS: Fast, Flexible, and Free. *J. Comput. Chem.* **2005**, *26*, 1701–1718.
- (36) Ballenegger, V.; Hansen, J. Dielectric Permittivity Profiles of Confined Polar Fluids. *J. Chem. Phys.* **2005**, *122*, 114711.
- (37) Stillinger, F. H.; Ben-Naim, A. Liquid-Vapor Interface Potential for Water. *J. Chem. Phys.* **1967**, *47*, 4431.
- (38) Wilson, M. A.; Pohorille, A.; Pratt, L. R. Surface-Potential of the Water Liquid Vapor Interface. *J. Chem. Phys.* **1988**, *88*, 3281.
- (39) Kirkwood, J. G. The Dielectric Polarization of Polar Liquids. *J. Chem. Phys.* **1939**, *7*, 911.
- (40) Fröhlich, H. *Theory of Dielectrics*; Clarendon Press: Oxford, U.K., 1949.
- (41) Bazant, M. Z.; Storey, B. D.; Kornyshev, A. A. Double Layer in Ionic Liquids: Overscreening versus Crowding. *Phys. Rev. Lett.* **2011**, *106*, 046102.
- (42) Bonthuis, D. J.; Netz, R. R. Dielectric Profiles and Ion-Specific Effects at Aqueous Interfaces. In *Proceedings of the Cecam Workshop "New Challenges in Electrostatics of Soft and Disordered Matter"*; Dean, D. S.; Dobnikar, J.; Naji, A.; Podgornik, R., Eds.; Pan Stanford: 2013.
- (43) Chandler, D. Physical Chemistry - Oil on Troubled Waters. *Nature* **2007**, *445*, 831–832.
- (44) Vinogradova, O. I. Drainage of a Thin Liquid-Film Confined between Hydrophobic Surfaces. *Langmuir* **1995**, *11*, 2213–2220.
- (45) Mamatkulov, S. I.; Khabibullaev, P. K.; Netz, R. R. Water at Hydrophobic Substrates: Curvature, Pressure, and Temperature Effects. *Langmuir* **2004**, *20*, 4756–4763.
- (46) Wu, P.; Qiao, R. Physical Origins of Apparently Enhanced Viscosity of Interfacial Fluids in Electrokinetic Transport. *Phys. Fluids* **2011**, *23*, 072005.
- (47) Hess, B. Determining the Shear Viscosity of Model Liquids from Molecular Dynamics Simulations. *J. Chem. Phys.* **2002**, *116*, 209.
- (48) Li, T.; Gao, J.; Szoszkiewicz, R.; Landman, U.; Riedo, E. Structured and Viscous Water in Subnanometer Gaps. *Phys. Rev. B* **2007**, *75*, 115415.
- (49) Bonthuis, D. J.; Rinne, K. F.; Falk, K.; Kaplan, C. N.; Horinek, D.; Berker, A. N.; Bocquet, L.; Netz, R. R. Theory and Simulations of

Water Flow through Carbon Nanotubes: Prospects and Pitfalls. *J. Phys.: Condens. Matter* **2011**, *23*, 184110.

(50) Van der Heyden, F. H. J.; Bonthuis, D. J.; Stein, D.; Meyer, C.; Dekker, C. Power Generation by Pressure-Driven Transport of Ions in Nanofluidic Channels. *Nano Lett.* **2007**, *7*, 1022–1025.

(51) Horinek, D.; Netz, R. R. Specific Ion Adsorption at Hydrophobic Solid Surfaces. *Phys. Rev. Lett.* **2007**, *99*, 226104.

(52) Horinek, D.; Herz, A.; Vrbka, L.; Sedlmeier, F.; Mamatkulov, S. I.; Netz, R. R. Specific Ion Adsorption at the Air/Water Interface: the Role of Hydrophobic Solvation. *Chem. Phys. Lett.* **2009**, *479*, 173–183.

(53) Levin, Y. Polarizable Ions at Interfaces. *Phys. Rev. Lett.* **2009**, *102*, 147803.

(54) Paillusson, F.; Blossey, R. Slits, Plates, and Poisson-Boltzmann Theory in a Local Formulation of Nonlocal Electrostatics. *Phys. Rev. E* **2010**, *82*, 052501.

(55) Bikerman, J. J. Structure and Capacity of Electrical Double Layer. *Philos. Mag.* **1942**, *33*, 384–397.

(56) Eigen, M.; Wicke, E. The Thermodynamics of Electrolytes at Higher Concentration. *J. Phys. Chem.* **1954**, *58*, 702–714.

(57) Kralj-Iglič, V.; Iglič, A. Influence of Finite Size of Ions on Electrostatic Properties of Electric Double Layer. *Electrotech. Rev. (Ljubljana, Slovenija)* **1994**, *61*, 127–133.

(58) Borukhov, I.; Andelman, D.; Orland, H. Steric Effects in Electrolytes: A Modified Poisson-Boltzmann Equation. *Phys. Rev. Lett.* **1997**, *79*, 00319007.

(59) Borukhov, I.; Andelman, D.; Orland, H. Adsorption of Large Ions from an Electrolyte Solution: A Modified Poisson-Boltzmann Equation. *Electrochim. Acta* **2000**, *46*, 221–229.

(60) Bazant, M. Z.; Kilic, M. S.; Storey, B. D.; Ajdari, A. Towards an Understanding of Induced Charge Electrokinetics at Large Applied Voltages in Concentrated Solutions. *Adv. Colloid Interface Sci.* **2009**, *152*, 48–88.

(61) Netz, R. R. Electrostatics of Counter-Ions at and between Planar Charged Walls: From Poisson-Boltzmann to the Strong-Coupling Theory. *Eur. Phys. J. E* **2001**, *5*, 557–574.

(62) Horinek, D.; Mamatkulov, S. I.; Netz, R. R. Rational Design of Ion Force Fields Based on Thermodynamic Solvation Properties. *J. Chem. Phys.* **2009**, *130*, 124507–124507.

(63) Huang, D. M.; Geissler, P. L.; Chandler, D. Scaling of Hydrophobic Solvation Free Energies. *J. Phys. Chem. B* **2001**, *105*, 6704–6709.

(64) Huang, D. M.; Cottin-Bizonne, C.; Ybert, C.; Bocquet, L. Aqueous Electrolytes near Hydrophobic Surfaces: Dynamic Effects of Ion Specificity and Hydrodynamic Slip. *Langmuir* **2008**, *24*, 1442–1450.

(65) Boda, D.; Henderson, D.; Eisenberg, B.; Gillespie, D. A Method for Treating the Passage of a Charged Hard Sphere Ion as It Passes through a Sharp Dielectric Boundary. *J. Chem. Phys.* **2011**, *135*, 064105.

(66) Bonthuis, D. J.; Horinek, D.; Bocquet, L.; Netz, R. R. Electrokinetics at Aqueous Interfaces without Mobile Charges. *Langmuir* **2010**, *26*, 12614–12625.

(67) Bonthuis, D. J.; Falk, K.; Kaplan, C. N.; Horinek, D.; Berker, A. N.; Bocquet, L.; Netz, R. R. Comment on “Pumping of Confined Water in Carbon Nanotubes by Rotation-Translation Coupling”. *Phys. Rev. Lett.* **2010**, *105*, 209401.

(68) Bikerman, J. J. Ionic Theory of Electroosmosis, the Current Flow and the Surface Conductivity. *Z. Phys. Chem., Abt. A* **1933**, *163*, 378–394.

(69) Bikerman, J. J. Die Oberflächenleitfähigkeit und ihre Bedeutung. *Kolloid-Z.* **1935**, *72*, 100.

(70) Lyklema, J. Surface Conduction. *J. Phys.: Condens. Matter* **2001**, *13*, 5027.

(71) Stein, D.; Kruithof, M.; Dekker, C. Surface-Charge-Governed Ion Transport in Nanofluidic Channels. *Phys. Rev. Lett.* **2004**, *93*, 035901.

(72) Bonthuis, D. J.; Netz, R. R. Unraveling the Combined Effects of Dielectric and Viscosity Profiles on Surface Capacitance, Electro-

Osmotic Mobility, and Electric Surface Conductivity. *Langmuir* **2012**, *28*, 16049–16059.

(73) Lyklema, J. On the Slip Process in Electrokinetics. *Colloids Surf., A* **1994**, *92*, 41–49.

(74) Lyklema, J.; Overbeek, J. T. G. On the Interpretation of Electrokinetic Potentials. *J. Colloid Sci.* **1961**, *16*, 501–512.

(75) Lyklema, J. *Fundamentals of Interface and Colloid Science*; Academic Press: London, 1995; Vol. II.

(76) Van der Heyden, F. H. J.; Stein, D.; Dekker, C. Streaming Currents in a Single Nanofluidic Channel. *Phys. Rev. Lett.* **2005**, *95*, 116104.

(77) Van der Put, A. G.; Bijsterbosch, B. H. Electrokinetic Measurements on Concentrated Polystyrene Dispersions and Their Theoretical Interpretation. *J. Colloid Interface Sci.* **1983**, *92*, 499–507.

(78) O'Brien, R. W.; Perrins, W. T. The Electrical Conductivity of a Porous Plug. *J. Colloid Interface Sci.* **1984**, *99*, 20–31.

(79) Zukoski, C. F.; a Saville, D. The Interpretation of Electrokinetic Measurements Using a Dynamic Model of the Stern Layer: I. The Dynamic Model. *J. Colloid Interface Sci.* **1986**, *114*, 32–44.

(80) Zukoski, C. F.; a Saville, D. The Interpretation of Electrokinetic Measurements Using a Dynamic Model of the Stern Layer: II. Comparisons between Theory and Experiment. *J. Colloid Interface Sci.* **1986**, *114*, 45–53.

(81) Dukhin, S. S.; Deryaguin, B. V. *Electrokinetic Phenomena. In Surface and Colloid Science*; Matijevic, E., Ed.; Wiley: New York, 1974; Vol. 7, p 356.

(82) Dukhin, S. S. Nonequilibrium Electric Surface Phenomena. *Adv. Colloid Interface Sci.* **1993**, *44*, 1–134.

(83) Lyklema, J.; Minor, M. On Surface Conduction and Its Role in Electrokinetics. *Colloids Surf., A* **1998**, *140*, 33–41.

(84) Hunter, R. J. The Significance of Stagnant Layer Conduction in Electrokinetics. *Adv. Colloid Interface Sci.* **2003**, *100*, 153–167.

(85) Hunter, R. J. *Foundations of Colloid Science*; Oxford University Press: Oxford, U.K., 2001.

(86) Löbbus, M.; Sonnfeld, J.; Van Leeuwen, H. P.; Volgelsberger, W.; Lyklema, J. An Improved Method for Calculating Zeta-Potentials from Measurements of the Electrokinetic Sonic Amplitude. *J. Colloid Interface Sci.* **2000**, *229*, 174–183.

(87) Minor, M.; Van der Linde, A. J.; Lyklema, J. Streaming Potentials and Conductivities of Latex Plugs in Indifferent Electrolytes. *J. Colloid Interface Sci.* **1998**, *203*, 177–188.

(88) Netz, R. R. Electrofriction and Dynamic Stern Layers at Planar Charged Surfaces. *Phys. Rev. Lett.* **2003**, *91*, 138101.

(89) Kim, Y.-W.; Netz, R. R. Electroosmosis at Inhomogeneous Charged Surfaces. *Europhys. Lett.* **2005**, *72*, 837–843.

(90) Kim, Y.-W.; Netz, R. R. Electro-Osmosis at Inhomogeneous Charged Surfaces: Hydrodynamic versus Electric Friction. *J. Chem. Phys.* **2006**, *124*, 114709.

(91) Herminghaus, S. A Generic Mechanism of Sliding Friction between Charged Soft Surfaces. *Phys. Rev. Lett.* **2005**, *95*, 264301.

(92) Erbas, A.; Horinek, D.; Netz, R. R. Viscous Friction of Hydrogen-Bonded Matter. *J. Am. Chem. Soc.* **2012**, *134*, 623–630.

(93) Chakraborty, J.; Dey, R.; Chakraborty, S. Consistent Accounting of Steric Effects for Prediction of Streaming Potential in Narrow Confinements. *Phys. Rev. E* **2012**, *86*, 061504.

(94) Von Hansen, Y.; Hinczewski, M.; Netz, R. R. Hydrodynamic Screening near Planar Boundaries: Effects on Semiflexible Polymer Dynamics. *J. Chem. Phys.* **2011**, *134*, 235102.